

RESEARCH ARTICLE

10.1002/2014JD022693

Key Points:

- An orographic cloud with large supercooled droplets was seeded with AgI nuclei
- Data from some radars point to a seeding-induced increase in precipitation rate
- It remains difficult to distinguish natural variations from AgI-induced effects

Correspondence to:

B. Pokharel,
bpokharel@uwyo.edu

Citation:

Pokharel, B., B. Geerts, and X. Jing (2015), The impact of ground-based glaciogenic seeding on clouds and precipitation over mountains: A case study of a shallow orographic cloud with large supercooled droplets, *J. Geophys. Res. Atmos.*, 120, 6056–6079, doi:10.1002/2014JD022693.

Received 7 OCT 2014

Accepted 20 MAY 2015

Accepted article online 23 MAY 2015

Published online 19 JUN 2015

The impact of ground-based glaciogenic seeding on clouds and precipitation over mountains: A case study of a shallow orographic cloud with large supercooled droplets

Binod Pokharel¹, Bart Geerts¹, and Xiaoqin Jing¹¹Department of Atmospheric Science, University of Wyoming, Laramie, Wyoming, USA

Abstract This paper examines the impact of ground-based glaciogenic seeding on a shallow, lightly precipitating orographic cloud with rather large (~35 μm) supercooled droplets. The storm was observed on 22 February 2012 as part of the AgI (silver iodide) Seeding Cloud Impact Investigation experiment in Wyoming. The cloud base (top) temperature was about −5°C (−12°C). Vertical velocity data from an airborne Doppler W-band (3 mm) profiling Wyoming Cloud Radar (WCR) indicate broad ascent due to the strong wind (20 m s^{−1}) impinging on the terrain and small pockets of intense updrafts. The large droplets, low droplet and ice particle concentrations, and strong updrafts lead to natural snow growth mainly by accretion (riming). The treated (seeded) period is compared with the preceding untreated period. The main target site, located on a mountain pass, was impacted by AgI seeding, according to a trace chemistry analysis of the falling snow. Data from three radar systems were used in the analysis of the impact of seeding on snow growth: the WCR, two Ka-band (1.2 cm) profiling Micro Rain Radars, and an X-band (3 cm) scanning polarization Doppler-on-Wheels radar. This case is complicated somewhat by a natural increase in cloud liquid water and in snow growth by riming, starting halfway during the seeding period, and continuing after seeding ended. Composite data from the centimeter-wave radar systems indicate an increase in low-level reflectivity during seeding, even after accounting for the natural trend observed in the upwind control region. A precipitation particle probe at the main target site shows an increase in concentration of both small and large hydrometeors.

1. Introduction

Winter precipitation in most of the interior western U.S. falls as snow over the mountains. This snowfall is responsible for most of the streamflow, including in the Colorado River. Although this region is rather arid, a significant amount of snow falls from orographic clouds. This snow typically has a low density, especially over the higher mountains, because the snow mainly grows by vapor deposition and aggregation [e.g., Steenburgh, 2014]. The cloud liquid water content (LWC) typically is quite low in mixed-phase clouds observed over mountains in the continental western U.S., below 0.5 g m^{−3} [Cooper and Vali, 1981; Rogers and Vali, 1987; Politovich and Vali, 1983]. On occasion the orographic clouds contain a larger amount of supercooled liquid water, and this water may occur mainly in the form of large droplets, giving rise to moderate to severe aircraft icing. Such icing can only be due to large droplets [Sand et al., 1984]. We have encountered such icing conditions on flights through shallow orographic clouds in Colorado, Wyoming, and Idaho. Here we report on one such event.

Supercooled water tends to be produced locally in persistent updraft upstream of terrain ridges. This has been confirmed by several studies using aircraft, microwave radiometers, and tower measurements over different mountain ranges in interior western U.S. [Hobbs, 1975; Sassen et al., 1986; Rauber and Grant, 1987; Politovich and Vali, 1983; Long and Huggins, 1992]. The droplets typically were small in these studies, with a mode diameter less than 15 μm. Ice concentration, crystal habits, and precipitation growth depend not just on available liquid water but also on droplet size [Rauber and Tokay, 1991]. The main snow growth mechanism shifts from diffusional to accretional growth as droplet size increases. That is because riming efficiency increases sharply from ~0 to ~1 as the droplet diameter increases from 5 to 20 μm for most ice crystal habits [Pruppacher and Klett, 1997; Wang and Ji, 2000]. Droplet size also affects ice crystal concentration, through secondary ice crystal generation by riming [Hallett and Mossop, 1974], but only at rather high temperatures: the Hallett-Mossop ice splintering mechanism rapidly ceases at temperatures below −8°C [e.g., Griggs and Choullarton, 1986].

The working hypothesis of glaciogenic cloud seeding is that when abundant amount of supercooled droplets are available with a limited amount of ice crystals, artificially injected ice nuclei produce more ice particles and enhance snow growth, at least if it is cold enough. For silver iodide (AgI) nuclei, a temperature lower than -5°C may be sufficient, but as temperature decreases to -12°C , the activation rate of AgI nuclei increases exponentially [DeMott, 1997].

In arid regions such as the western U.S., cold-season orographic clouds have been seeded with glaciogenic material such as AgI nuclei for more than a half century, with the intent to increase precipitation [Bruintjes, 1999]. But cloud seeding efficacy and optimal seeding conditions remain poorly understood [Garstang *et al.*, 2005]. A 2003 National Research Council report [National Research Council, 2003] laments the lack of progress in cloud seeding research and recommends both statistically rigorous precipitation studies, as well as cloud and precipitation process studies utilizing novel instruments and high-resolution numerical simulations.

The 2007–2014 Wyoming Weather Modification Pilot Project (WWMPP) [Breed *et al.*, 2014] is the most recent statistically rigorous precipitation impact study. The 2012 AgI Seeding Cloud Impact Investigation (ASCII-12) was conducted in the context of the WWMPP to use novel instruments to explore how glaciogenic seeding of orographic clouds affects cloud and precipitation processes. ASCII-12 was conducted over the Sierra Madre in southern Wyoming during January–March 2012 [Geerts *et al.*, 2013].

The present paper is the third ASCII-12 case study. The first case study [Pokharel *et al.*, 2014a, hereafter referred to as PGJ14] examines stratiform orographic precipitation under strong winds on 21 February 2012, while the second study [Pokharel *et al.*, 2014b, hereafter referred to as P14] examines precipitating shallow orographic convection observed under weaker winds, on 13 February 2012. In these two cases smaller cloud droplets were encountered. The modus droplet diameter was $\sim 20\ \mu\text{m}$ in the PGJ14 case, while it was no larger than $25\ \mu\text{m}$ in the convective clouds described in P14. Data from several particle probes indicate that ice crystal concentrations increased downwind of the AgI generators during seeding in these two cases (PGJ14 and P14). Radar data reveal an increase in low-level reflectivity in the stratiform case (PGJ14) as well as in five other stratiform cases in ASCII-12 [Jing *et al.*, 2015]. The impact on low-level reflectivity in the convective case (P14) is not obvious, possibly because the impact region is further downwind (X. Jing and B. Geerts, Dual-polarization radar data analysis of the impact of ground-based glaciogenic seeding on winter orographic clouds, Part II: Convective clouds, *Journal of Applied Meteorology Climatology*, in review, 2015), although enhanced silver (Ag) concentrations were measured in falling snow at the target site.

The present paper uses the same instruments to focus on a shallow, persistent, highly sheared and rather well-mixed orographic cloud with large cloud droplets (modus $\sim 35\ \mu\text{m}$). The cloud top temperature was no colder than -12°C . At this temperature natural ice nucleation is quite rare [e.g., Grant and Elliott, 1974; DeMott *et al.*, 2010]. The liquid water content was unusually high, which favors seeding efficacy [e.g., Li and Pitter, 1997; Givati and Rosenfeld, 2005; Zipori *et al.*, 2012; Xue *et al.*, 2013a]. There was no cloud layer aloft from which ice crystals could fall into the lower orographic cloud (the seeder-feeder mechanism).

The experimental design for this study is described in section 2. Cloud and atmospheric conditions for this case are described in section 3. Data from three different radar systems and from a disdrometer are used to explore the seeding impact, in sections 4 and 5, respectively. The findings are discussed and summarized in sections 6 and 7, respectively.

2. Experimental Design and Instruments

The ASCII-12 project is described in Geerts *et al.* [2013]. The experimental design and instruments are detailed in PGJ14 and P14. Here we highlight the measurements and instruments used for this study. ASCII-12 was designed to measure clouds and precipitation both during natural conditions and while AgI nuclei were injected into the boundary layer upstream of the Sierra Madre. Measurements were made both upstream and downstream of the AgI generators. The upstream measurements are considered “control,” to evaluate the natural variation, and downstream data are treated as “target,” affected both by natural trends and by seeding. The measurement sites as well as the aircraft flight strategy are shown in Figure 1.

Several ground-based and airborne platforms were deployed on 22 February 2012. The University of Wyoming King Air (UWKA) was equipped with the profiling 3 mm wavelength (W-band) Wyoming Cloud Radar (WCR), the 355 nm Wyoming Cloud Lidar (WCL), several cloud microphysical in situ probes, and state parameter probes

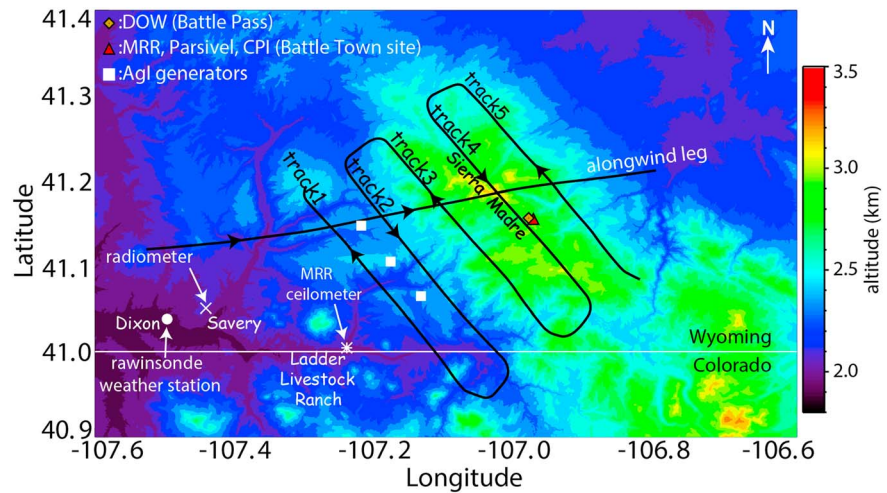


Figure 1. ASCII-12 experimental design map, showing UWKA flight tracks, and ground-based instruments. The terrain elevation is shown in the background. The solid black lines show parts of the 22 February 2012 flight track, including one of the ladder patterns, with track labels (#1–5), and an along-wind leg.

[Wang et al., 2012]. Two particle probes are used here, the Cloud Imaging Probe (CIP), measuring particles in the range 25–800 μm , and the Cloud Droplet Probe (CDP), measuring droplets in the range 3–50 μm . The CIP count in the first two bins is less certain and may include large droplets, so it is ignored. The CDP with pointed asymmetric tips is not impacted significantly by ice particle shattering [Lance et al., 2010].

The WCR's great strength is that its vertical velocity and reflectivity profiles depict storm vertical structure from echo top down to ~ 30 m above ground level (agl) in the presence of cloud or precipitation particles. The two main drawbacks of the WCR, at least for quantitative reflectivity analysis, are the attenuation by liquid water absorption, and the scattering by large particles in the Mie regime. For droplets smaller than 100 μm diameter, the power extinction coefficient at 94 GHz is $4.8 \text{ dB km}^{-1} \text{ g}^{-1} \text{ m}^{-3}$ of cloud water [Vali and Haimov, 1999]. The Rayleigh scattering model breaks down starting with particles of size $D \sim 25\%$ of the wavelength. Reflectivity increases with D^6 in the Rayleigh regime and asymptotically with just D^2 in the Mie regime. For W-band, that threshold size is 0.76 mm, but for X-band (3 cm), it is 7.6 mm.

The UWKA flight level was not constant on 22 February 2012. The design flight level was 13 kft (~ 3.9 km mean sea level (msl)), the lowest allowed in cloud over the Sierra Madre, but large droplets were encountered, resulting in severe icing conditions at 13 kft. Thus, the flight level was increased to just above cloud. Because the optical array and some other particle probes had become ice-covered, and because much of the flight level was above clouds, little useful information in situ cloud physics probes are available later in the flight.

Several instruments operated on the ground on 22 February 2012. A scanning dual-polarization X-band Doppler-on-Wheels (DOW) radar was located at Battle Pass, a continental divide pass (elevation 3034 m msl) (Figure 1), with excellent views toward the Agl generators on the SW (upwind) side, and toward the east (lee) side. The DOW conducted full volume scans every 8 min, alternating with a 1.5 min series of Range Height Indicator scans along the wind direction.

Instruments were located on top of a scaffold structure surrounded by trees, some 500 m downwind of the DOW. This site, referred to as Battle Town site, hosted a profiling 24 GHz Micro Rain Radar (MRR), several snow measuring instruments including a Parsivel disdrometer [Löffler-Mang and Joss, 2000; Yuter et al., 2006] and a Cloud Particle Imager (CPI) [Lawson et al., 2006], and an Environmental Technology Inc. (ETI) precipitation gauge. Manual snow photography was conducted at this site, and fresh snow samples were collected to analyze concentrations of silver and other trace elements. A second MRR operated at Ladder Livestock ranch (Figure 1) upstream of the Agl generators. It is treated as a control measurement.

The upstream environment was monitored by a second MRR, a ceilometer, a passive microwave radiometer, an automated weather station, and rawinsondes. The radiometer, located at Savery (Figure 1) and pointed at

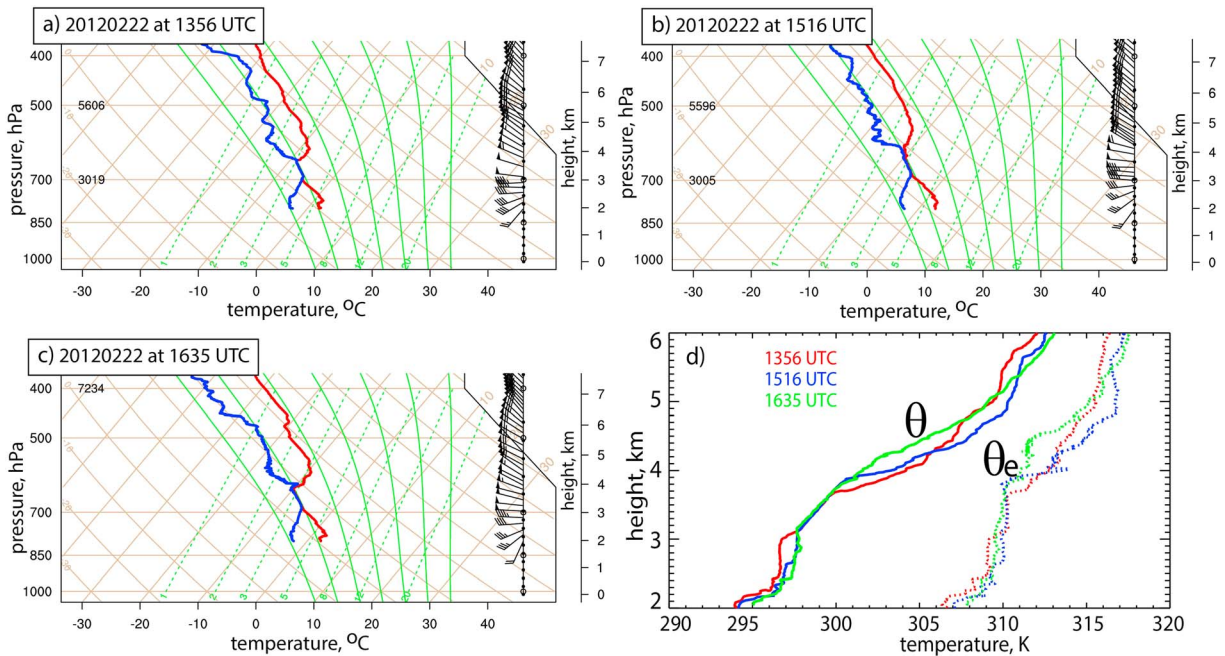


Figure 2. Skew-T log-p display of rawinsonde data from Dixon (a) during the pre-SEED period and (b and c) during the SEED period, in IOP12. The red lines show the temperature, and the blue lines show the dewpoint. A full barb equals 5 m s^{-1} (~10 kts). (d) Vertical profiles of potential temperature θ and equivalent potential temperature θ_e for these three soundings.

low elevation angle to the NE over the Sierra Madre, mainly provides cloud liquid water path (LWP). Three GPS rawinsondes were released from Dixon (Figure 1) on 22 February 2012.

A series of five geographically fixed aircraft tracks (a “ladder”) was flown four times. The ladder was flown in an upstream direction (Figure 1) to minimize possible contamination by aircraft-induced ice particles [Rangno and Hobbs, 1983]. Flight track #1 was upstream of the three Agl generators, thus serving as control measurement. WCR data from the four tracks downstream of the generators (#2–5) are treated as target measurement. Tracks #2–3 are located upstream of the Sierra Madre mountain crest, track #4 is close to the mountain crest, and track #5 is in the lee. Two ladders were flown before Agl generators activation at 15:10 UTC; this period is referred as pre-SEED. Next, an along-wind leg (Figure 1) was flown, allowing time for Agl nuclei to mix in the boundary layer and to reach the target region. Next, two more ladders were flown, a period is referred as SEED. Legs #2 and #1 were not flown on the last ladder because airframe ice accumulation had reduced the aircraft’s endurance.

3. Atmospheric Conditions and Cloud Characteristics

3.1. Upstream Conditions

Synoptically, the ASCII-12 intensive operations period #12 (IOP12) on 22 February 2012 occurred in the wake of a deep upper level trough that had moved through the previous day. A northwesterly upper level jet was located over northeast Wyoming. At low levels cold air had spread over the northern and central Plains. Orographic precipitation occurred over mountain ranges from the Cascades to the Sierra Madre. Steady, light snowfall occurred over the Sierra Madre during this case.

The cloud top temperature was no colder than -12°C (Figure 2), and subsidence above the cloud layer implied no natural seeding from aloft, as confirmed by WCR reflectivity profiles. The lowest saturated level in the sounding was about -5°C . The sounding-based lifting condensation level (LCL) temperature is 1–2 K higher (Figure 3b), because the lowest ~250 m of atmosphere above Dixon appears to be trapped in the valley, in which Dixon lies (Figure 2d), making a surface-based LCL unrealistically low. The sounding-based LCL is estimated from the average specific humidity and potential temperature between 100 and 500 m agl.

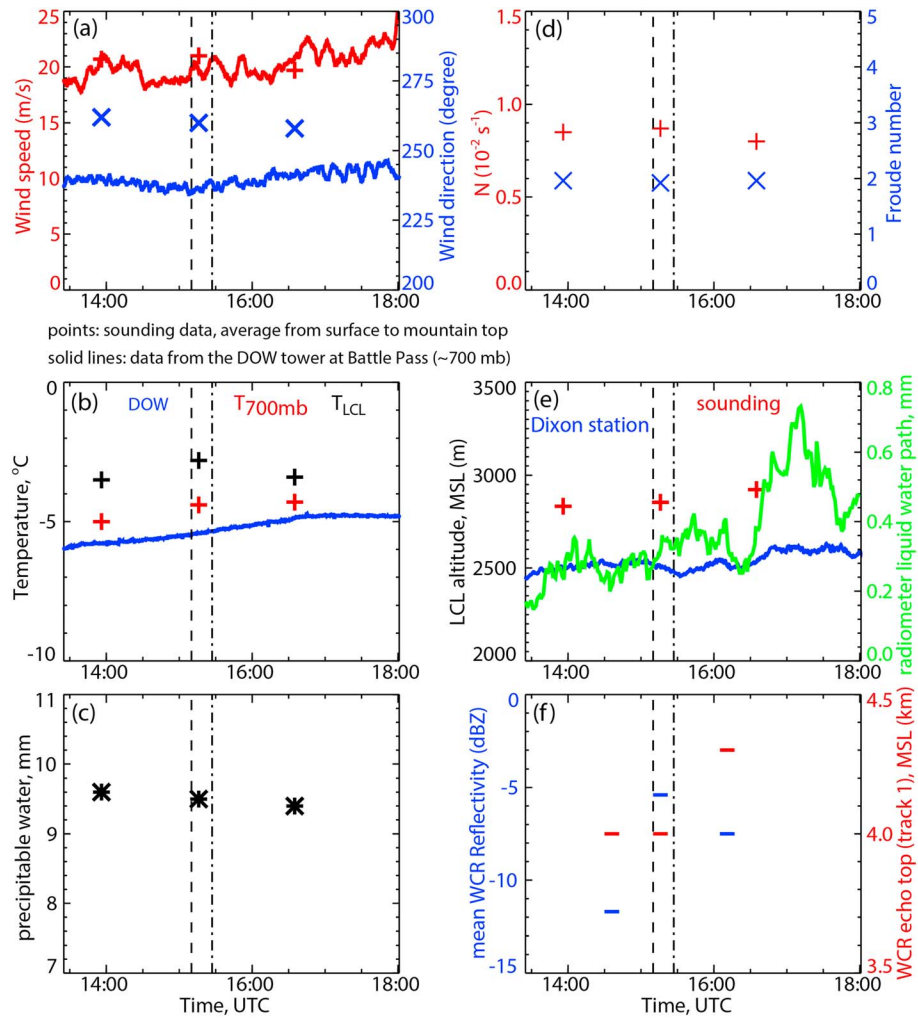


Figure 3. Evolution of several atmospheric parameters during the course of IOP12, as measured by rawinsondes, weather stations in the upwind valley and on the mountain, and WCR. The surface station data at Dixon and Battle Pass (DOW) have a 1 min resolution, with wind measurement at 10 m and temperature and humidity at 2 m. The vertical dashed line and vertical dash-dotted line in all panels show the AgI generators start time and the estimated arrival time of the AgI plume at Battle Pass, respectively.

If the cloud layer is well-mixed, then the -5 to -12°C temperature range is quite suitable for AgI-based seeding, because the probability of AgI-mediated ice nucleation rapidly increases in that temperature range [DeMott, 1997]. The LWP was higher than any other ASCII-12 case (0.3–0.7 mm; Figure 3e). The low-level wind direction (Figure 3a) was suitable to examine seeding impact because the AgI generators were upwind of the main target site at Battle Pass. The surface wind was rather strong, $\sim 20\text{ m s}^{-1}$ at 10 m above the DOW at Battle Pass (Figure 3a).

The soundings reveal a very shallow ($\sim 0.25\text{ km}$) stable layer near the surface, then a $\sim 0.8\text{ km}$ deep well-mixed boundary layer, and a nearly moist-neutral, saturated layer above that, up to $\sim 4\text{ km}$ ($\sim 620\text{ mb}$) (Figure 2d). The three AgI generators were located $\sim 0.5\text{ km}$ above the valley floor in Dixon, i.e., above the shallow stable layer. This cloud layer was capped by an inversion. Significant veering occurred from the surface to cloud top, with strong winds. Conditions were rather steady for the three soundings (Figure 2), except that the cloud base and top, and the inversion above cloud top, lifted a little from the first to the third sounding.

3.2. Storm Evolution During the IOP

We now examine several atmospheric variables measured at different locations from different instruments (Figure 3). The reasons for this analysis are to describe ambient and cloud conditions and to examine storm steadiness during a 4 h period, in which the treated period (SEED) is compared to the untreated

Table 1. Definition of Pre-SEED, SEED, and Post-SEED Periods for the 22 February 2012 IOP^a

Instrument	Pre-SEED		SEED		Post-SEED	
	Start	Stop	Start	Stop	Start	Stop
WCR/UWKA	14:05:50	15:18:35	15:38:00	16:36:43	N/A	N/A
UWKA cross-wind tracks	L1: T5-T1 L2: T5-T1		L3: T5-T1 L4: T5-T3		N/A	N/A
MRR, Parsivel	13:27:00	15:27:00	15:28:00	17:28:00	17:29:00	19:29:00
DOW	13:07:54	15:31:45	15:31:46	17:53:15	N/A	N/A

^aThree Agl generators were operating from 15:10 to 17:10 UTC \pm a few minutes. The times are in UTC (HH:MM:SS). L refers to a ladder pattern, consisting of 5 tracks (T), as shown in Figure 1. The UWKA flew an along-wind leg after completing two ladder patterns, thereby creating a buffer period between pre-SEED and SEED (15:19–15:38 UTC). No such period is assumed for the instruments at Battle (MRR, Parsivel, and DOW), but a \sim 20 min advection time between the Agl generators and Battle is applied.

period (pre-SEED). The pre-SEED and SEED periods for the UWKA, the DOW, and the Battle Town site instruments are given in Table 1. These periods vary for the different platforms, depending on flight operations and advection time from the Agl generators to the target site.

The surface wind speed at Battle Pass (\sim 20 m s⁻¹) matches the wind speed measured by rawinsondes at the same level (700 mb) just upwind of the Sierra Madre (Figure 3a). The wind direction is more southerly at Battle Pass (compared to that from the soundings), because of terrain channeling (Figure 1). Since the observed wind speed and direction are rather constant, the atmospheric stability and flow condition also remain steady during the IOP (Figure 3d). The bulk Brunt-Vaisala frequency N is calculated from the surface to mountain top level, as a weighted mean of the dry value from the surface to the LCL and the moist value above the LCL, the latter using the equation in *Kirschaum and Durran* [2004]. Its value ($N \sim 0.3 \cdot 10^{-2} \text{ s}^{-1}$) would be lower still if there was no shallow stable layer in the Dixon valley. This N and the surface to mountaintop mean wind speed U are used to compute the bulk Froude number Fr ($Fr = U/(NH)$, where H is the height of the mountain above the upwind plains). For each of the three soundings, $Fr \sim 2$ ($Fr \sim 6$ if the shallow stable layer is ignored), suggesting that the low-level flow above the valley inversion was unblocked and the Agl nuclei were readily advected over the mountain.

Slight warming (\sim 1 K/4 h) occurred during the IOP (Figure 3b) due to warm air advection and/or daytime heating. The precipitable water (integrated water vapor, calculated from soundings) remains steady (Figure 3c). Consistent with these changes, the LCL height increased a little, as calculated both from the soundings and from the Dixon surface weather station data (Figure 3e). (The latter is less representative because of the shallow valley inversion.) The LCL is about 2.9 km msl, i.e., \sim 0.4 km above the height of the Agl generators. This corresponds well with the mean ceilometer cloud base height at Ladder Livestock ranch (Figure 1).

Overall, ambient conditions were quite steady during this IOP.

3.3. Cloud and Precipitation Properties

Clouds and precipitation were not as steady, confirming that these are more structured, “noisy” fields. The radiometer LWP was rather steady until 16:30 UTC, and then nearly doubled (Figure 3e). The WCR mean echo top and mean near-surface reflectivity along track #1 (upwind of the Agl generators) reveal a positive trend (Figure 3f), but a single track of data may not be very representative, and track #1 was flown only once during SEED, before the jump in LWP.

High amounts of cloud liquid water were measured also by in situ probes (Figure 4a), before the flight level was lifted to just above cloud top. The average (maximum) flight-level in-cloud liquid water content (LWC) during the first pass along track #3 was 0.52 (1.03) g m⁻³ (Figure 4a). This was not due to a high droplet concentration, which was just \sim 31 cm⁻³ (Figure 4b). This is lower than typical values observed in other ASCII cases (B. Pokharel and B. Geerts, manuscript in preparation, 2015) and over mountains in southern Wyoming (100–500 cm⁻³) [*Politovich and Vali*, 1983]. Rather, the high LWC is due to unusually large droplets, with mode diameter of \sim 35 μ m, according to the CDP (Figure 4c). The typical droplet mode diameter is 10–15 μ m in this continental region [*Politovich and Vali*, 1983]. The large cloud droplets

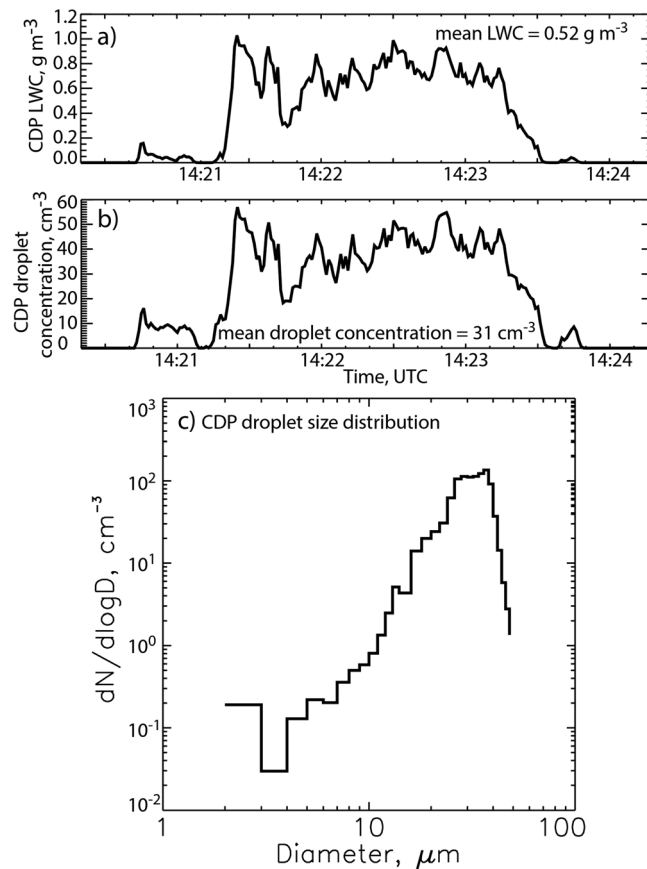


Figure 4. (a) Liquid water content, (b) droplet concentration, and (c) droplet size distribution measured by the CDP early in the flight (ladder #1) on track #3 (Figure 1) at a flight level of 4.4 km msl. Average values are also shown in Figures 4a and 4b.

produced rimed snow crystals, many of them round, some cone-shaped, according to imagery from the airborne cloud imaging particle (CIP) (not shown). Particle concentrations >62 μm in size were about 30 L⁻¹. Track #3 was flown again partly in-cloud at 16:35 UTC (ladder #4). The CDP was not compromised by icing and measured a similar LWC and drop size distribution as it did earlier (Figure 4b). Thus, these unusual cloud conditions likely persisted throughout the IOP. Conditions suitable for large-drop formation are a warm cloud top temperature, a low droplet concentration [Politovich, 1989], and significant wind shear in the cloud layer, causing turbulence and fine-scale inhomogeneous mixing [Pobanz et al., 1994]. These three conditions applied in this case (Figures 2–4).

Heavily rimed ice crystals were seen also on the ground at Battle Town site, by the CPI and in crystal photography (Figure 5). The habits of some of the crystals imaged by the CPI are difficult to characterize due to riming. The CPI imagery reveals large needles or columns, plates, rosettes, and irregularly shaped crystals. All these habits can form at the observed temperatures

(−5 to −12°C) [Korolev and Issac, 1999; Lundqvist et al., 2012]. The CPI imaged many aggregates, and some nearly spherical graupel particles. Two snow photographs included in Figure 5 show graupel ~2 mm in diameter. Heavily rimed particles were observed during both pre-SEED (photo at 14:26 UTC in Figure 5) and SEED (photo at 17:07 UTC) periods. Such particles have a higher density and have a higher fallspeed [Locatelli and Hobbs, 1974]; thus, they yield a higher precipitation rate for a given radar reflectivity [Raubert and Tokay, 1991; Rasmussen et al., 2003]. This should be considered when converting observed reflectivity values, shown below, to precipitation rates.

3.4. WCR Along-Wind Transect

A flight track along the low-level wind was flown between the pre-SEED and SEED flight patterns (Figure 1). The vertical profile of WCR reflectivity and Doppler velocity, and WCL backscatter power and depolarization ratio along this track are shown in Figure 6. The orographic cloud upwind and over the Sierra Madre on 22 February 2012 was quite shallow and contained some ice crystals upwind of the AgI generators (Figure 6a). Reflectivity values above about −10 dBZ can only be due to ice particles [Wang and Geerts, 2003], as drizzle-size droplets, >100 μm diameter, were not observed at flight level (before the particle probes became covered with ice). The ice particle concentration was quite small: concentrations around 20–25 L⁻¹ were encountered on the most upwind track with cloud penetration (track #2) on the second and third passes, according to the CIP in the bins starting at 62 μm. No liquid-only clouds were encountered at flight level.

The WCR (hydrometeor) vertical velocity is shown in Figure 6b. Note that the color key bar is centered at −1 m s⁻¹ to account for the typical fall speed of (unrimed) snow. Given the observed significant riming, the fallspeed probably was larger, and upward air motion may not be limited to the blue regions alone.

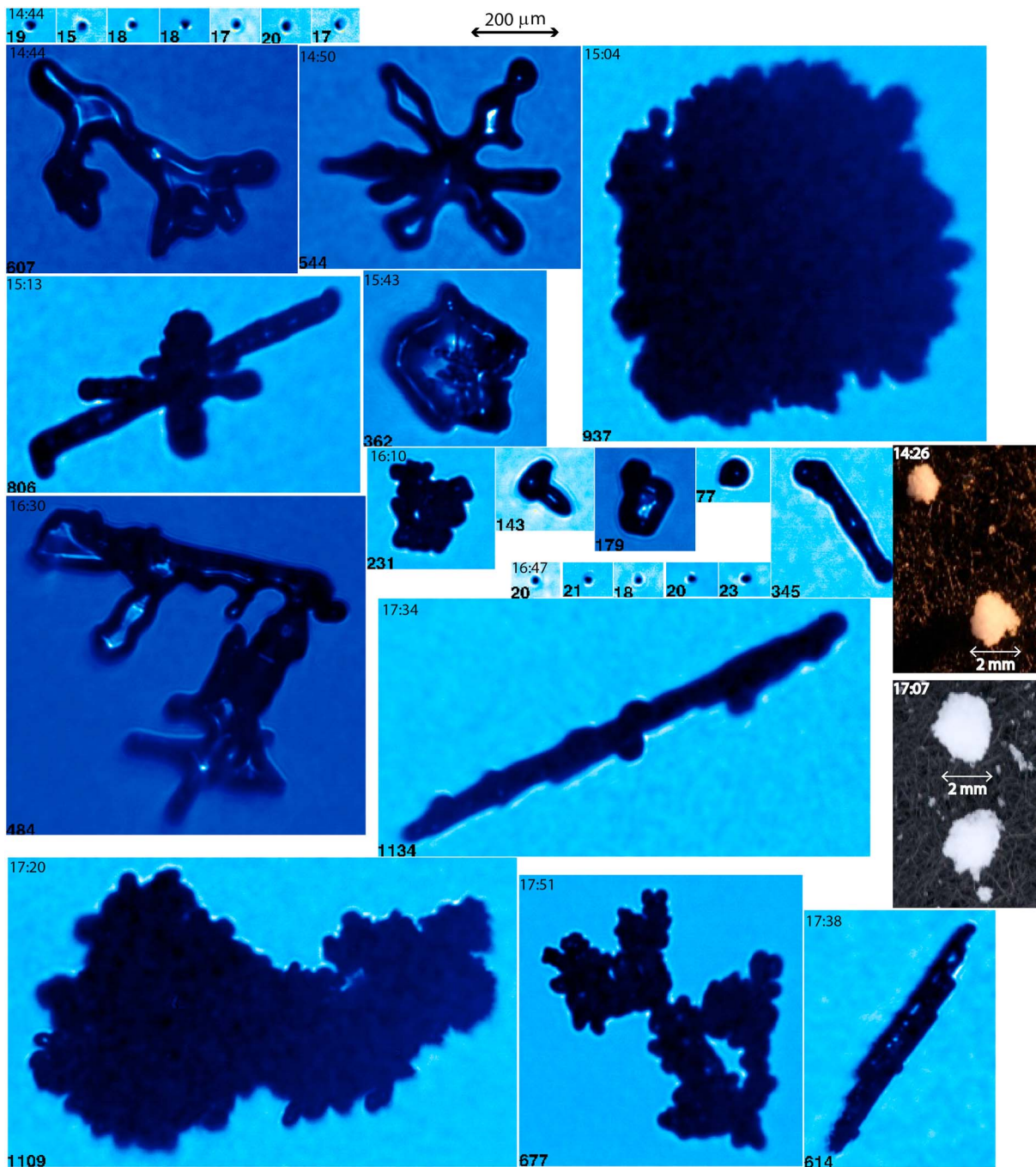


Figure 5. A sampling of snow crystal and water droplet images taken by the Cloud Particle Imager (CPI—blue background) and manually by a camera (two images with a black velvet background on the right) at Battle Town site (Figure 1) during IOP12. The scale is shown at the top for the CPI images and inside the image for camera photos. The time (UTC) is shown in the upper left corner of each sample. The number in lower left corner shows the maximum dimension of the measured particles, in microns.

The air vertical velocity measured by a gust probe is shown as well, at the flight level. It is centered at 0 m s^{-1} , but otherwise uses the same color scale as that for WCR velocities.

Two scales of vertical motion are evident in Figure 6b. Most important are the larger-scale terrain-driven eddies, with updrafts (downdrafts) penetrating to cloud top in areas of ascending (descending) terrain, on account of the strong wind blowing from the left. An example can be found around “hill A,” at $x = 35 \text{ km}$ in Figure 6b. In upslope regions the WCR vertical velocity is $1\text{--}2 \text{ m s}^{-1}$ near cloud top. This corresponds with

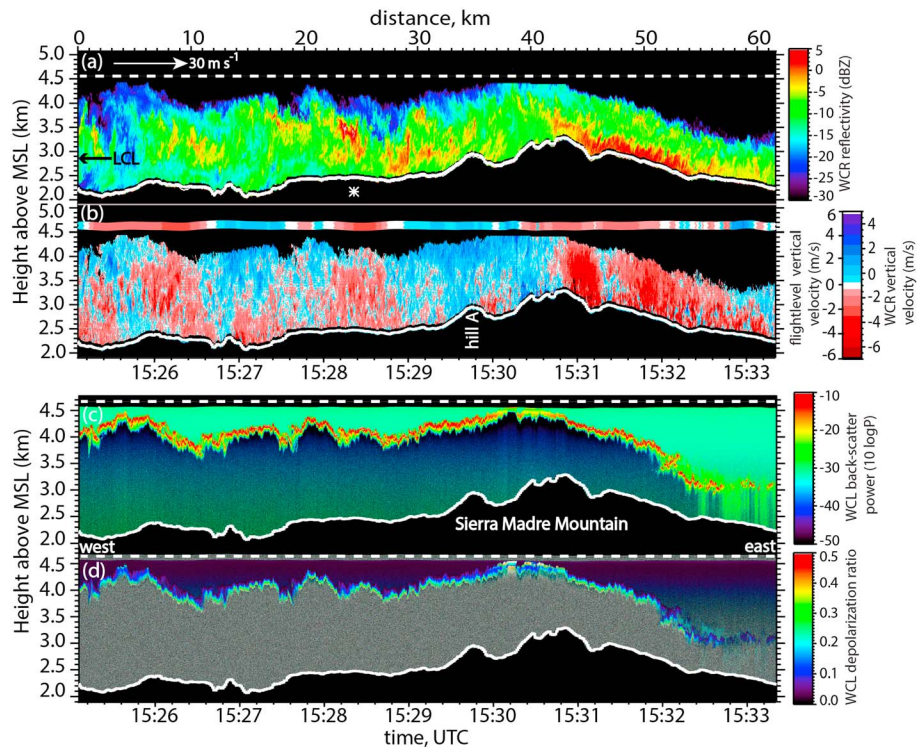


Figure 6. WCR and WCL transect for the along-wind flight leg over the Sierra Madre shown in Figure 1. The wind direction is from left (260°, west) to right (80°, east). (a) WCR reflectivity and (b) WCR hydrometeor vertical velocity plus air vertical velocity measured at flight level; (c) WCL backscatter power and (d) WCL depolarization ratio. The dashed white line in Figures 6a, 6c, and 6d is the UWKA flight level, and the white line below is the terrain profile. The measured cloud is shallow and located below flight level only. The white arrow on the left side of Figure 6a is the sounding-estimated cloud base (LCL), and the asterisk below the terrain in Figure 6a shows the approximate projection of the three Agl generators in this transect.

an updraft of (at least) $2\text{--}3\text{ m s}^{-1}$, which is consistent with the wind speed ($\sim 20\text{ m s}^{-1}$) and the terrain slope ($\sim 1:10$, locally steeper). Such terrain-driven layer ascent is quite possible given the near-neutral lapse rate and lack of θ_e increase in the cloud layer above the valley inversion (Figure 2d). The terrain-driven vertical pattern persists at flight level, 4.5 km msl (Figure 6b), but is suppressed and more wave-like on account of the overlying stable layer.

Second, fine-scale updraft and downdraft near the surface are due to shear-driven turbulence in the planetary boundary layer (PBL), as evident from near-surface WCR vertical velocity power spectra (not shown) [Geerts *et al.*, 2011]. Remarkably, these small eddies are found not just near the surface, but all the way to cloud top, presumably because of the strong wind and near-neutral lapse rate (Figure 2). In essence, this orographic cloud is a boundary layer cloud.

Especially at smaller-scale upwind of the crest, the WCR vertical velocity w_{hydro} often exceeds the typical fallspeed of unrimed snow; in other words, ice crystals initially are carried upward ($w_{\text{hydro}} > 0\text{ m s}^{-1}$). This allows for growth by accretion (riming) in the presence of large droplets [e.g., Houze, 1993]. The apparent increase in w_{hydro} with height upwind of the crest (Figure 6b) may be less a flow feature and more a fallspeed signature due to an increasing riming fraction at low levels above cloud base. This will be revisited later.

The WCR vertical velocity field (Figure 6b) suggests rather effective vertical turbulent mixing of air from near the surface into the cloud layer (from $\sim 2.9\text{ km msl}$ to echo top). This is important for seeding impact because of the rather high cloud base temperature. Since Agl nuclei have no significant fallspeed, an average updraft of $1.0\text{--}1.5\text{ m s}^{-1}$ suffices to bring Agl nuclei from the generators (shown as an asterisk in Figure 6a) to cloud top above the crest, about 18 km to the east, assuming the observed wind profile (Figure 2).

The thin layer of high lidar backscatter power (Figure 6c), with a low depolarization ratio (Figure 6d) and complete signal attenuation below, clearly indicates a liquid water cloud top. This cloud top is best defined upwind of the mountain crest. The cloud top backscatter power gradually decreases in the lee, and the lidar signal penetrates deeper, suggesting that the cloud gradually becomes devoid of liquid water near the east end of the transect. In cases with lower upwind LWP, this leeward transition occurs over a shorter distance (e.g., PGJ14).

The vertical motions are likely fine-scale shear-driven turbulence in the lowest 0.5–1.0 km and embedded weak convection above the boundary layer. This interpretation is consistent with the soundings (Figure 2). The patches of higher reflectivity aloft (Figure 6a) probably are due to convective updrafts. Forward camera footage aboard the UWKA suggests somewhat cumuliform, solid cloud tops. In the lee of the main crest, subsidence prevails, and higher reflectivity occurs near the ground.

In short, the vertical velocity pattern is supportive of efficient mixing of ground-released AgI nuclei into cloud, up to levels cold enough for effective AgI-mediated ice nucleation (around -8°C), but cloud ice was present before and upwind of the AgI seeding.

3.5. Orographic Flow and Precipitation

The four WCR reflectivity transects collected along flight track #4 are shown in Figure 7. This track approximately aligns with the crest of the Sierra Madre (Figure 1), and is about 15 km downstream of the AgI generators. The upper (lower) two panels in Figure 7 are measured during pre-SEED (SEED). The star symbols in lower two panels show the projected locations of the AgI generators, assuming the direction of the mean low-level wind. Light snowfall fell across the entire transect during all four passes. (Note that the flight level varies between passes.) Echoes were tilted to the right (SE) by the prevailing NW shear (Figure 2). Higher reflectivity repeatedly is observed on the right (SE) side, where the terrain rises more steeply to the crest (Figure 1). Reflectivity generally decreases toward the ground, even though the LCL was below ground level along most of track #4. The echo depth (~ 1.5 km) and average reflectivity did not change much during the 2.3 h period. No well-defined plumes of enhanced reflectivity can be seen along the projected AgI plume locations in the third and fourth transects (Figures 7c and 7d), consistent with other case studies (PGJ14 and P14). Since a seeding impact is not obvious in WCR reflectivity transects, the reflectivity data are composited for all flight sections downwind of AgI generators in frequency by altitude diagrams (FADs) [Yuter and Houze, 1995]. The FADs for the two periods (SEED and pre-SEED) are shown in Figure 8. These diagrams show the frequency of a reflectivity value at certain height agl, normalized by the total frequency in all bins. Orographic snow growth is quite obvious with higher mean low-level reflectivity values over the mountain (target) than the foothills (control) (Figures 8a and 8d).

Reflectivity tends to decrease toward the ground in the lowest 1 km in both regions. In the control region this may be due to sublimating snow because the cloud base is ~ 600 m agl. An explanation is less obvious in the target region, whose elevation is largely above the LCL. There the low-level reflectivity may be affected significantly by absorption by liquid water. At flight level, an average of 0.53 g m^{-3} of cloud water was encountered in cloud along track #3 on the first and last ladder patterns (Figure 4). At lower levels the LWC probably was lower, vanishing altogether at cloud base. An average LWC of 0.25 g m^{-3} implies 2.4 dB km^{-1} in two-way attenuation. So the attenuation-corrected near-surface reflectivity in the target region (Figure 8d) probably is 2–3 dB higher.

The hydrometeor vertical velocity w_{hydro} (Figures 8b and 8e) shows significant spread associated with terrain-forced eddies and turbulence (section 3.4). The average w_{hydro} in the target region (orange line in Figure 8e) decreases from 0 m s^{-1} near cloud top (suggesting an average updraft of at least 1 m s^{-1}) to -2.5 m s^{-1} in the lowest 800 m. In all likelihood this indicates an increase in particle terminal velocity toward the ground due to riming. This decrease in w_{hydro} from cloud top toward the ground is only about half as large in the control region, and the mean w_{hydro} is larger (less negative) in the control region, suggesting less riming there. This suggests that fewer large supercooled droplets occurred in the foothills region and that droplets grew in the orographic cloud, likely because a low concentration of cloud condensation nuclei (not measured) and a dearth of ice particles (section 3.4). This implies a rather inefficient Bergeron diffusional growth process. The slight decrease in w_{hydro} from pre-SEED to SEED in the control and target regions (Figures 8b and 8e) may indicate more riming during SEED, consistent with the observed increase in LWP (Figure 3e).

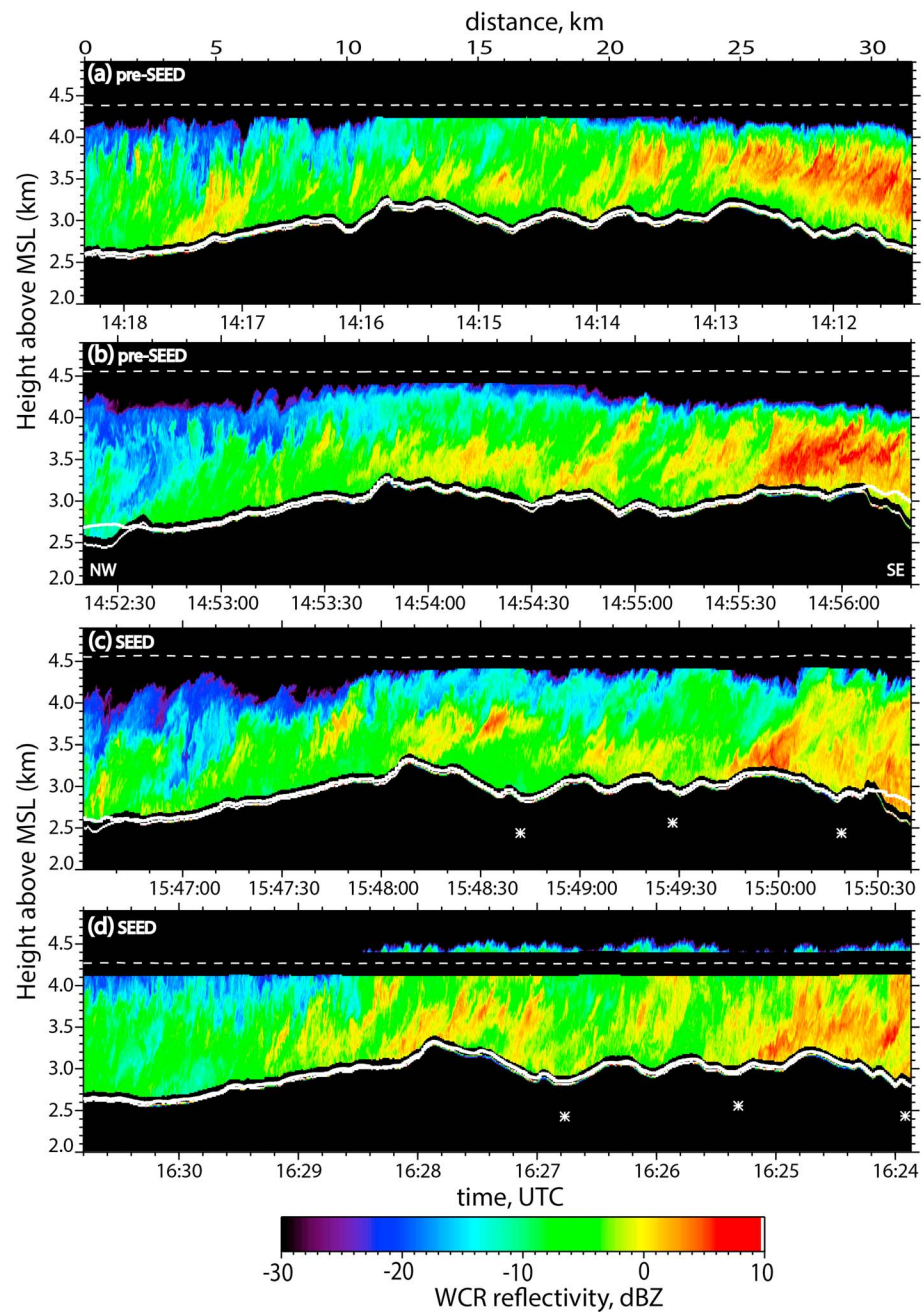


Figure 7. Example UWKA radar reflectivity transects, collected along flight track #4 (Figure 1) on 22 February 2012. All transects are from (left column) NW to (right column) SE, the direction of the low-level shear (Figure 2). The upper two transects were flown during pre-SEED; the lower two transects were flown during SEED. The asterisks in lower two panels show the location and actual elevation of the three AgI generators (~21 km into the page) projected on this transect, following the mean low-level wind. The actual terrain, shown by the white line in all panels, is not aligned with the WCR ground level at the left and right corners in Figures 7b and 7c due to aircraft roll.

4. Seeding Impact Detection

The hydrometeor size distributions are characterized in terms of a single, integral parameter, radar reflectivity, using three different radar systems, complementary in their wavelength, viewing perspective, spatial coverage, and thus definition of the control and target regions. The SEED versus pre-SEED conditions are compared in both regions for the three radar systems.

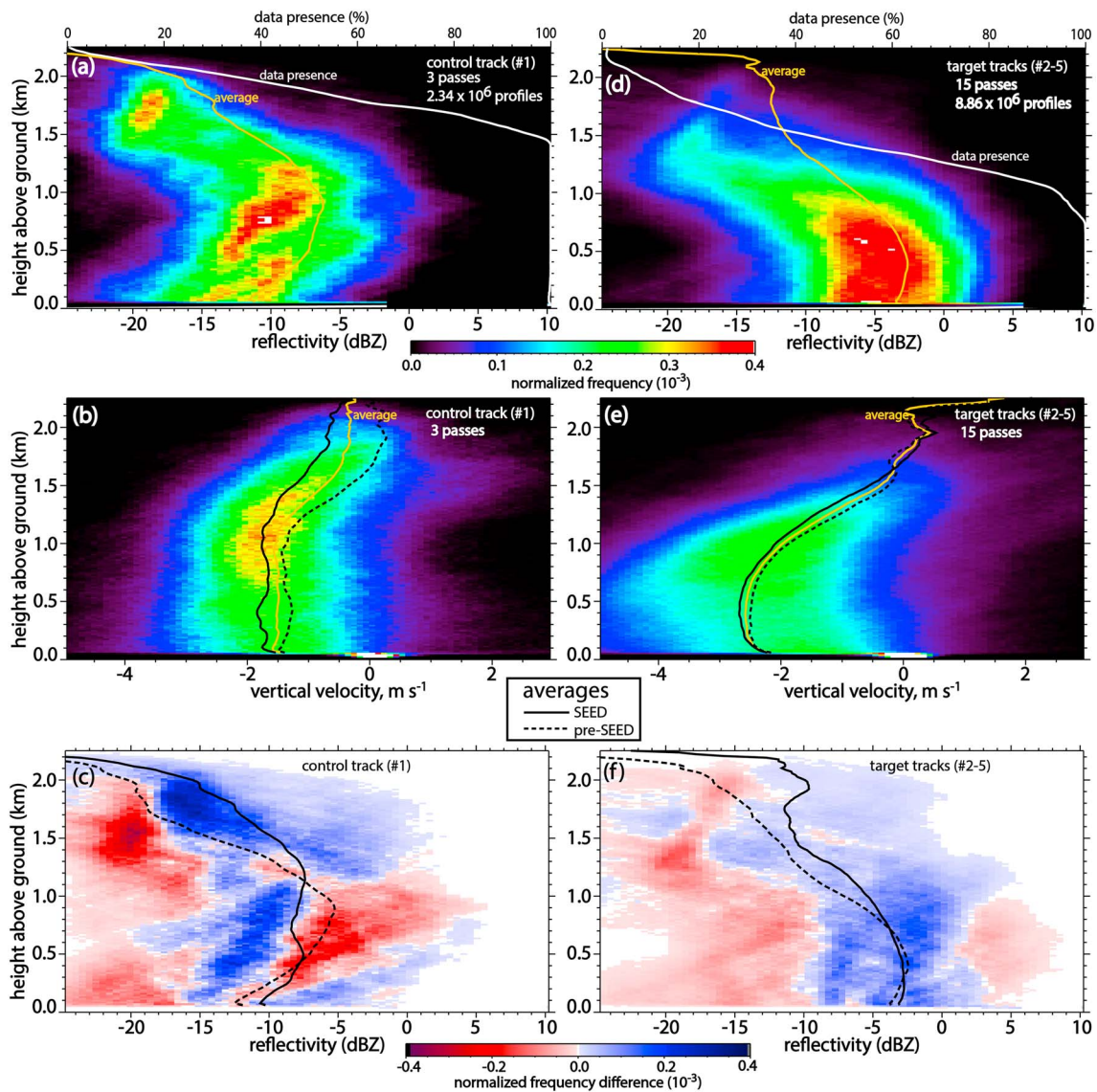


Figure 8. Normalized frequency by altitude diagrams (FADs) of (top row) WCR reflectivity and (middle row) vertical velocity for the 22 February 2012 flight. The left column applies to track #1 (control), the right column to the four tracks downwind of the AgI generators (target). The mean reflectivity profile (orange lines) and the “data presence” profile, i.e., the percentage of WCR range gates with radar echo as a function of height (white line), are also shown in the top row. The average vertical velocity profile (orange line) and average profiles during the pre-SEED (dashed line) and SEED (solid line) periods are also shown in the middle row. (c and f) The reflectivity difference FAD (SEED – pre-SEED), with the average reflectivity profiles for the two periods (black lines).

4.1. WCR Perspective

The temporal difference (SEED – pre-SEED) in the control region (Figure 8c) may not be representative because it is based on just two passes in pre-SEED, and one pass in SEED. The WCR sampling is quite limited, in a narrow beam along the flight track, and thus some aliasing may occur when the reflectivity field is patchy (as in this case) and few flight legs are composited. The temporal difference is more representative in the target region (Figure 8f), with 7–8 passes in each period. In both regions the echo top height increases from pre-SEED to SEED, consistent with changes in the upwind soundings (Figure 2). The mean near-surface reflectivity (Z) is slightly higher during SEED than pre-SEED in the target region (solid versus dashed lines in Figure 8f), but the same applies in the control region. To accommodate the concern that the control region may not be representative, one can increase the control region to include track #2, which is just 3 km downwind of the AgI generators and unlikely to witness any seeding impact, with this strong wind. The Z difference FADs in the enlarged control region (tracks #1 and 2) and a shrunk target

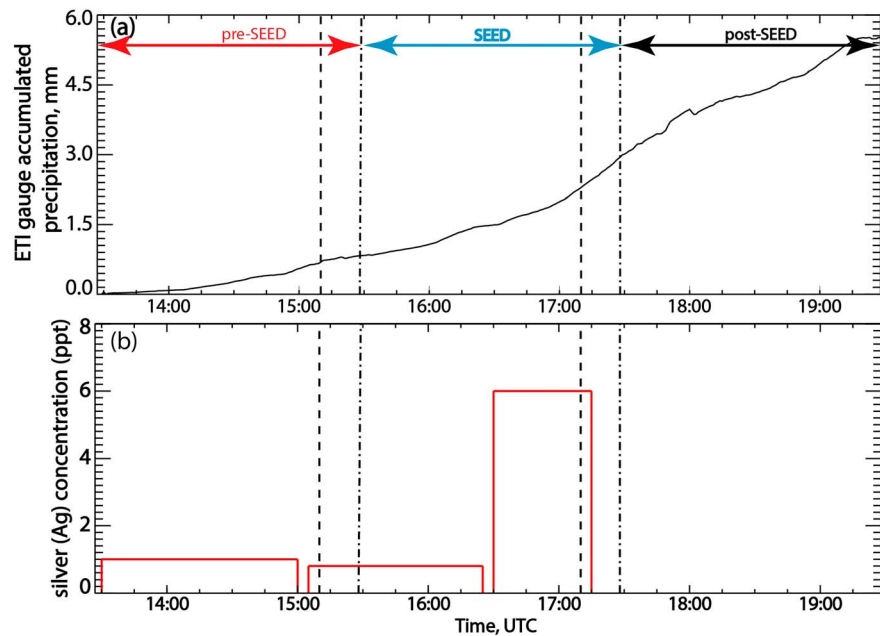


Figure 9. Time series of (a) accumulated precipitation measured by an ETI snow gauge and (b) silver (Ag) concentration in parts per trillion (ppt) from three fresh snow samples collected during IOP12 at Battle Town site. The width of the histogram shows the duration of snowfall collected. The vertical dashed lines in both panels show the AgI generators start/end times. The dash-dotted lines are the estimated times of the AgI plume presence over Battle Pass; they separate the three periods, pre-SEED, SEED, and post-SEED.

region (tracks #3–5) are very similar to those shown in Figures 8c and 8f (not shown). The same similarity applies for a lateral control region (northern parts of tracks #2–5) compared to a core target region (southern parts of tracks #2–5).

In short, there is no evidence of any significant impact of seeding on W-band reflectivity.

4.2. MRR Perspective

Two MRRs were deployed, one upwind of the AgI generators, and one downwind, at Battle Town site (Figure 1). Measurements at Battle Town site can be used to analyze seeding impact only if the site is impacted by seeding. Silver (Ag) and other trace elements in freshly fallen snow were measured at Battle Town site. One snow sample was collected during pre-SEED, and two during SEED. The Ag concentration was less than 2 ppt (parts per trillion) in first two samples but exceeded 6 ppt in the last sample (Figure 9). This enhancement was not found in other trace elements such as Cesium and Rubidium (which naturally correlate well with Ag and vary due to varying atmospheric mineral aerosol loads); thus, it is likely that the extra Ag in snow is due to AgI seeding. Further evidence for this comes from an analysis of expected plume advection patterns (Figure 10, insert). If we define an AgI plume as a 20° cone aligned with the mean low-level wind and spreading from any of the three AgI generators, then at least one plume (the northernmost one) intercepts Battle Town site, for all three soundings (Figure 2). Thus, it is likely that snow falling at Battle Town site was impacted by AgI seeding.

The MRR data were reprocessed to remove any noise following *Maahn and Kollias* [2012]. Effectively, the first two range gates had to be discarded; thus, the minimum data level is 450 m agl for the MRR at Battle Pass and 700 m for the upwind valley MRR, with a larger gate spacing. Low-level snow growth is evident at Battle Pass, yet low-level sublimation is likely in the upstream valley, with much lighter snowfall on the ground (mean profiles in Figure 10), consistent with WCR data. The mean low-level MRR reflectivity at Battle Pass also is much (15–20 dB) higher than that of the WCR in the target region (Figure 8d), on account of both the larger fraction of Mie scatterers and the larger signal absorption by liquid water at W-band. The reflectivity difference FADs indicate an ~6 dBZ reflectivity increase at Battle Pass in the lowest 1 km during SEED, compared to pre-SEED, but no significant change in low-level reflectivity in the valley MRR, located upwind

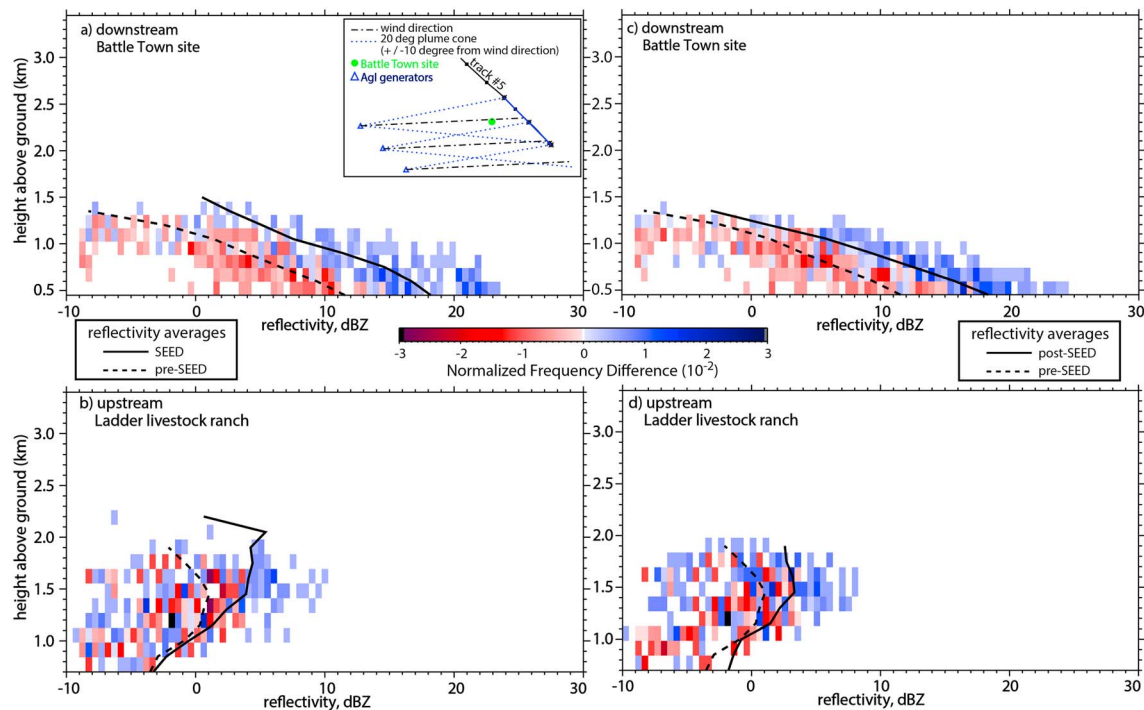


Figure 10. The left column shows the normalized reflectivity difference FAD for (SEED – pre-SEED) for (a) the downstream MRR (target) and (b) the upstream MRR (control). The right column shows the same but for the difference (post-SEED – pre-SEED). A schematic map with 20° wide cones representing Agl plumes with the target location and a flight track is inserted in Figure 10a. The solid and dashed lines show the average values during SEED and pre-SEED (post-SEED and pre-SEED) in the left (right) column, respectively. The pre-SEED, SEED, and post-SEED periods are given in Table 1.

of the Agl generators. This apparently positive seeding impact Ka-band Z disagrees with findings from the WCR transects.

Interestingly, this increase in Battle Pass MRR reflectivity persists into the post-SEED period, i.e., the 2 h period following SEED (Figure 10c). The low-level Z change in the control region is much smaller (Figures 10b and 10d). Starting around 1.5 h after the end of SEED, the Battle Pass MRR reflectivity decreases to values close to those observed during pre-SEED. It is possible that notwithstanding the strong wind, the Agl nuclei remain airborne in the target area for up to 2 h after seeding. Note that no other radar data were available during post-SEED (Table 1).

4.3. DOW Perspective

A dual-polarization DOW conducted volume scans from Battle Pass at 10 min intervals during the pre-SEED and SEED periods (Table 1). The additional dimension (3-D, compared to the 2-D WCR transects and 2-D MRR time-height transects) provides a richer, more representative data set. Also, at X-band all hydrometeors fall in the Rayleigh regime, and power loss due to liquid water absorption is insignificant. Therefore, the DOW is superior to the MRR and especially the WCR in detecting Agl-mediated snow growth. The main drawback of the DOW data is the lack of data near the ground in complex terrain, although from Battle Pass the DOW had excellent low-elevation coverage to the west and east (Figure 11). The discontinuities in height of the lowest unblocked beam in Figure 11 are due to shifts in the lowest beam not blocked by the terrain near the DOW. The lowest elevation angle of the DOW volume coverage pattern is –1° (unblocked only in two sectors, to the WSW and E to NE) incrementing by 1° initially. The higher terrain to the NW and S of the DOW at Battle Pass is cleared only at 3° and 6°, respectively (Figure 11). Details of the DOW data processing, ground clutter removal, and noise removal can be found in *Jing et al.* [2015].

Three regions of DOW volume data are defined for the purpose of examining the seeding impact (Figure 11). The upwind control area is defined as a region upstream of the three Agl generators where lowest unblocked DOW beam is not higher than 1.0 km above the terrain. Its lateral boundaries are aligned with the low-level mean wind and intersect the northern and southern generator locations. The upwind (lee) target area is

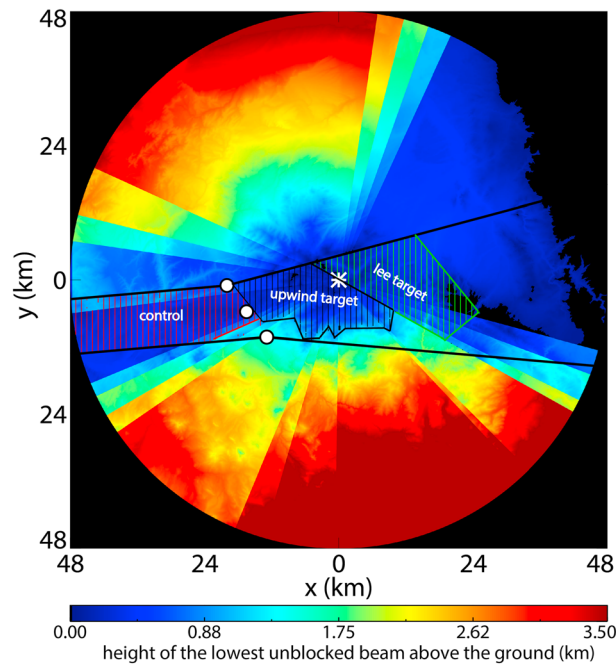


Figure 11. Height (km agl) of the lowest unblocked beam agl from the DOW radar, located at Battle Pass (Figure 1). Three vertically hatched regions used in the analysis of the seeding impact are also shown: the upstream control region (red hatching), the “upwind target” region (black) upwind of the mountain crest, and the “lee target” region (green) in the lee.

near the ground is about the same as the mean MRR Z at Battle Town site (Figure 10c), but the latter decreases more rapidly with height. Examining the mean reflectivity profiles, we again see basic orographic changes, i.e., a dramatic increase in low-level Z from the foothills (control) to the mountain (upwind target) and a rapid Z decrease from upwind to lee target areas at low levels (~ 0.5 – 1.5 km agl) (Figures 12a–12c). In this layer the WCR vertical velocity FAD along track #5 (Figure 1) shows strong subsidence (not shown).

The reflectivity tends to increase between pre-SEED and SEED in all regions below ~ 2 km. However, the increase in mean Z during SEED in the control area is small compared to that in the upwind target area. The low-level Z increment (SEED versus pre-SEED) becomes smaller in the lee target area. We map out DOW average Z and ZDR below 1.5 km agl in Figure 13. The data density is highest near the DOW and lowest at great range, especially at places where the lowest unblocked DOW beam is high agl. Precipitation (or its surrogate, low-level Z) is patchy in the control area but widespread over the mountain during pre-SEED (Figure 13a). The rapid precipitation decrease in the lee is obvious in both periods. Precipitation becomes widespread and more intense in the control area during SEED (Figure 13b), consistent with the FAD (Figure 12a). But stronger enhancement is found starting near the Agl generators and dropping off rapidly a few kilometer downwind of the crest (Figure 13c). In short, the DOW data indicate a positive impact, consistent with the MRR. We define this “positive impact” as a low-level precipitation rate increase (SEED – pre-SEED) in the target area, relative to any change in the control area over the same period.

The ZDR values are distributed around 0.0 dB in the target regions (Figures 12e and 12f). These values are lower than in most stratiform cloud cases in ASCII, where the low-level ZDR averages around 0.4–0.7 dB [Jing *et al.*, 2015]. This suggests that particles are more spherical and randomly oriented than in the typical ASCII stratiform cases, where unrimed dendrites and aggregates are dominant [Jing *et al.*, 2015]. This is consistent with the rimed particles observed on the ground (Figure 5). The ZDR values are about 0.3 dB higher over the mountain than the foothills or the lee (Figure 13d). This difference is small but above the DOW’s ZDR accuracy. It indicates that particles are more horizontally oriented over the mountain, such as by aggregation.

ZDR does not change significantly in the control region during the IOP (Figure 12d). Yet in both target regions, ZDR decreases by ~ 0.2 dB in the lowest 1 km agl during SEED (Figures 12e and 12f). This decrease

downstream of the three generators and upstream (downstream) of the mountain crest. These two target regions are separated to assess seeding impact as a function of fetch and to examine the seeding impact on opposite sides of the mountain crest. The northern boundary of the target area is defined by the wind direction plus 10° to represent plume dispersion from the northernmost generator. Other parts of the target area boundaries are based on the elevation of the lowest unblocked DOW beam (not higher than 1.0 km above the terrain) and the distance from the generators (no more than 36 km).

The DOW reflectivity Z and differential reflectivity (ZDR) data are composited for two periods (pre-SEED and SEED) and three regions (control, upwind target, and lee target) and the resulting reflectivity and ZDR difference FADs (SEED minus pre-SEED) are shown in Figure 12). Almost no data remain below ~ 500 m agl after ground clutter removal in the control region (Figure 12a). The mean DOW Z over the target region

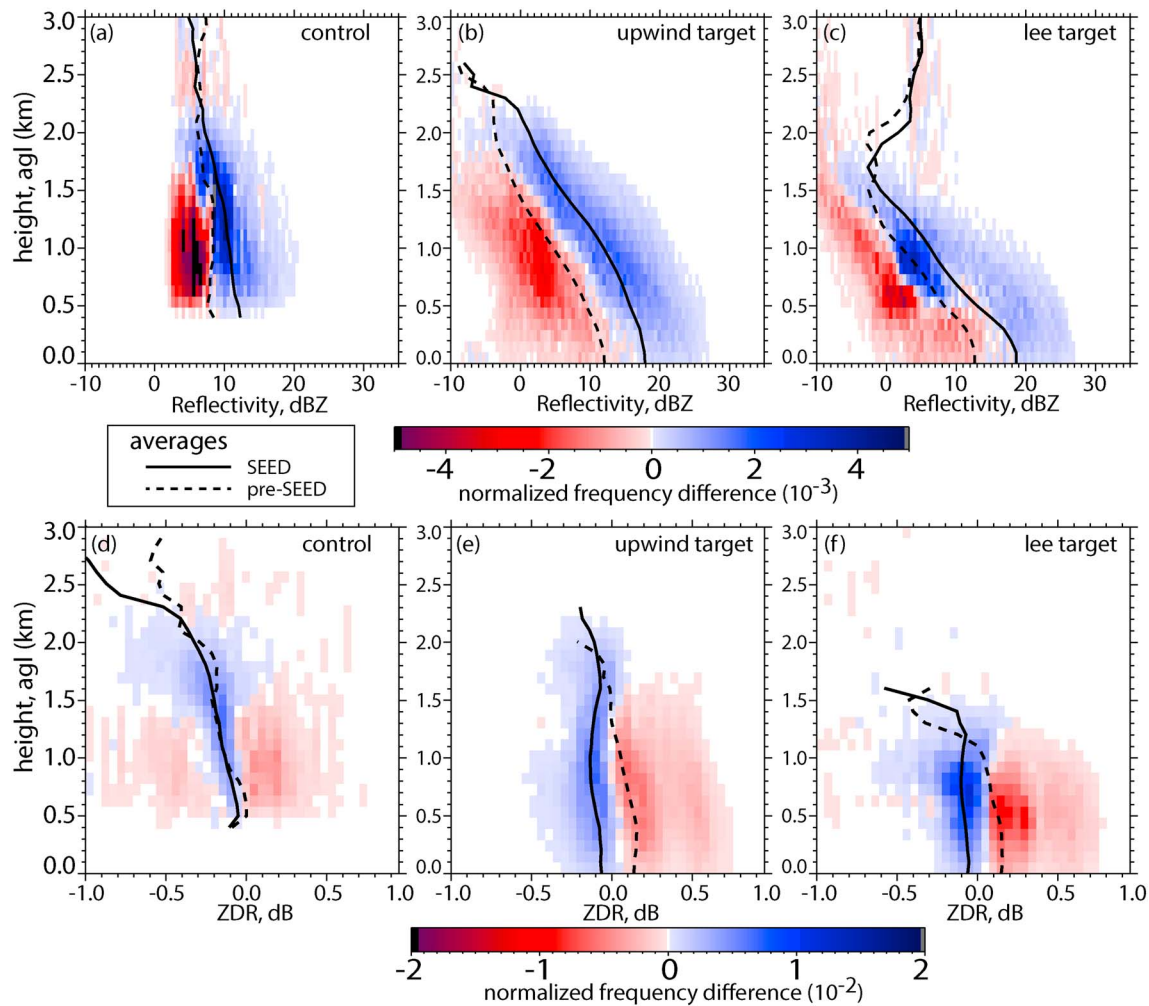


Figure 12. The top row shows the DOW radar reflectivity difference FADs (SEED – pre-SEED) measured in the (a) control region, (b) upwind target region, and (c) lee target region. The bottom row shows the DOW differential reflectivity (ZDR) difference FADs (SEED – pre-SEED) measured in the (d) control region, (e) upwind target region, and (f) lee target region.

is concentrated over the mountain (Figure 13e). This indicates that the larger particles, which dominate Z and ZDR, are more spherical during SEED. This suggests more riming during SEED, which is consistent with the increase in LWP in the second half of SEED (Figure 3e).

To examine the variation of ZDR for a given value of Z (which is a measure of hydrometeor size at the high end of the size distribution), the ZDR frequency distribution is plotted as function of Z in Figure 14, specifically for the target region. The bin resolutions of Z and ZDR are 1 and 0.05 dB, respectively. ZDR is narrowly distributed and does not increase with Z (Figures 14a and 14b), unlike the typical ASCII stratiform cases [Jing et al., 2015]. ZDR actually becomes lower for Z values above ~10 dBZ, which likely is due to graupel.

Significantly lower ZDR values are encountered for any Z value during SEED, resulting in a clear dipole in the frequency difference plot (Figure 14c). This ZDR analysis is more meaningful because it is independent of any change in Z from pre-SEED to SEED (Figures 12b and 12c). The decrease in ZDR during SEED probably is associated with heavier riming due to the higher LWC observed during that period (mainly after 16:30 UTC; Figure 3e).

4.4. Multiradar Changes in Reflectivity Profiles

As mentioned before, the changes in WCR reflectivity profiles (SEED – pre-SEED in the target region) do not match those from the centimeter-wave radars (MRR and DOW), which is quite plausible since they have

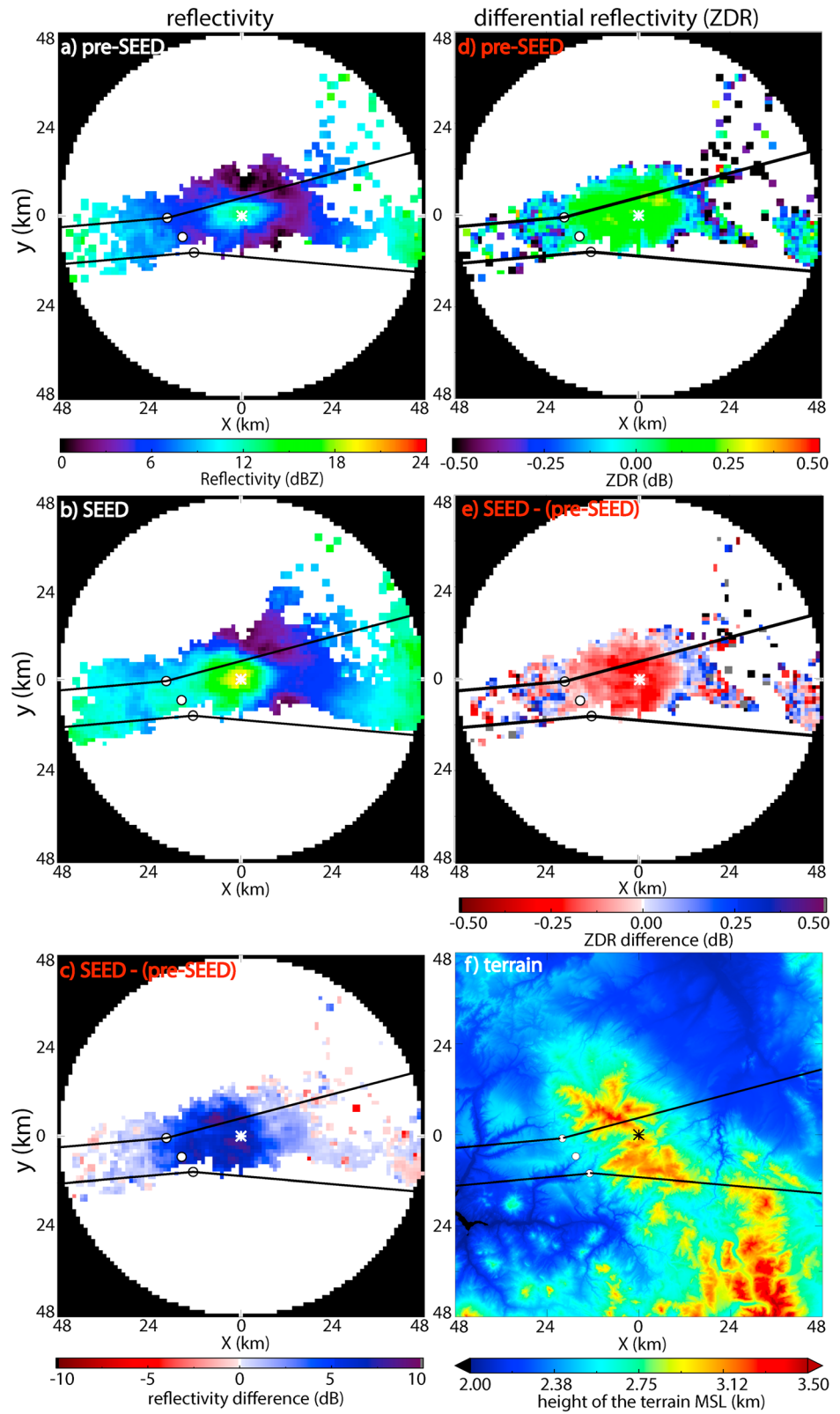


Figure 13. The left plots show the average DOW reflectivity below 1.5 km agl during (a) pre-SEED, (b) SEED periods, and (c) the mean reflectivity difference. The two upper right plots show the average ZDR below 1.5 km agl during (d) pre-SEED and (e) the mean ZDR difference (SEED – pre-SEED). The lower right plot (Figure 13f) shows the terrain map. In all these maps, the white circles are the Agl generators and the asterisk is the DOW location. The black lines are as in Figure 11.

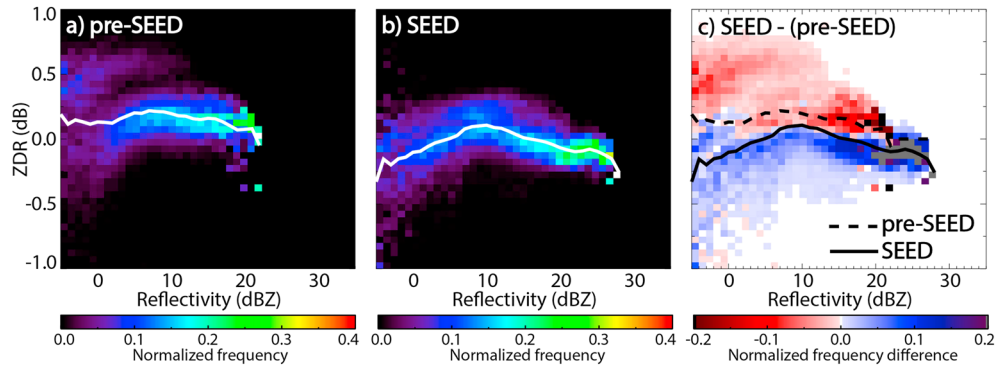


Figure 14. Normalized frequency of reflectivity (Z) by ZDR for the target (upwind plus lee) region, during (a) the SEED period and (b) the pre-SEED period in IOP12. (c) The frequency difference (SEED – pre-SEED) is also shown. Only points within 1.5 km agl are included in the count. The white lines in Figures 14a and 14b represent the average ZDR for any Z value. They are repeated as black lines in Figure 14c.

different sensitivities to cloud LW and large-particle scattering properties, different target/control areas, and slightly different SEED/pre-SEED periods (Table 1).

To summarize, we compare the average reflectivity profiles from the three radar systems in Figure 15. Both the simple temporal difference (SEED – pre-SEED) in the target region and a double difference are plotted. The double difference, called reflectivity impact parameter (ZIP) in PGJ14, is defined as the difference between the downstream (target) average reflectivity change (SEED – pre-SEED) and that upwind of the AgI generators (control), i.e.,

$$ZIP = \Delta dBZ_T - \Delta dBZ_U \tag{1}$$

where $\Delta dBZ = \Delta dBZ_S - \Delta dBZ_N$ and subscript *S* (*N*) refers to SEED (pre-SEED), while subscript *T* (*U*) refers to treated or target (untreated or control).

This ZIP can be expressed as a relative change in precipitation rate (*R*, mm h⁻¹), if we assume a relationship between *R* and *Z* (mm⁶ m⁻³). First we define the precipitation impact factor (PIF) as a relative change in *R* (SEED versus pre-SEED) in the target area compared to the same relative change in the untreated area. PIF is calculated as

$$PIF = \frac{\frac{R_{S,T}}{R_{N,T}}}{\frac{R_{S,U}}{R_{N,U}}} \tag{2}$$

Assuming the standard *Z-R* relationship of the form $R = aZ^b$, where *a* and *b* are constants, PIF is related to ZIP, as shown in PGJ14:

$$PIF = 10^{\left(\frac{b \times ZIP}{10}\right)} \tag{3}$$

A range of values of *b* have been found observationally for centimeter-wave radars [e.g., Austin, 1987] and millimeter-wave radars [e.g., Matrosov, 2007]. We use a single value (*b* = 0.7) for the three radars in Figure 15, for the simple reason that the emphasis is not on the magnitude of the precipitation change, but rather on its sign. Values of ZIP > 0 (and thus PIF > 1) imply a positive reflectivity (snowfall) trend in the target region, relative to the control region, from pre-SEED to SEED. ZIP profiles may yield an insight into attribution: changes near the surface may be attributable to ground-based seeding, while those aloft are more likely to be natural.

5. Surface Snow Measurement

As discussed in section 4.2, snow samples collected at Battle Town site indicate that the main target site likely was impacted by AgI seeding. Snowfall was measured by a Parsivel disdrometer and an ETI gauge at this site. The Parsivel provides snow concentrations in 32 size bins ranging from 0.062 to 24.5 mm in diameter.

The time series of Parsivel snow particle concentration reveals a positive trend during the IOP (Figure 16b). The concentration only tapers off in the post-SEED period. The number of small snow particles increases

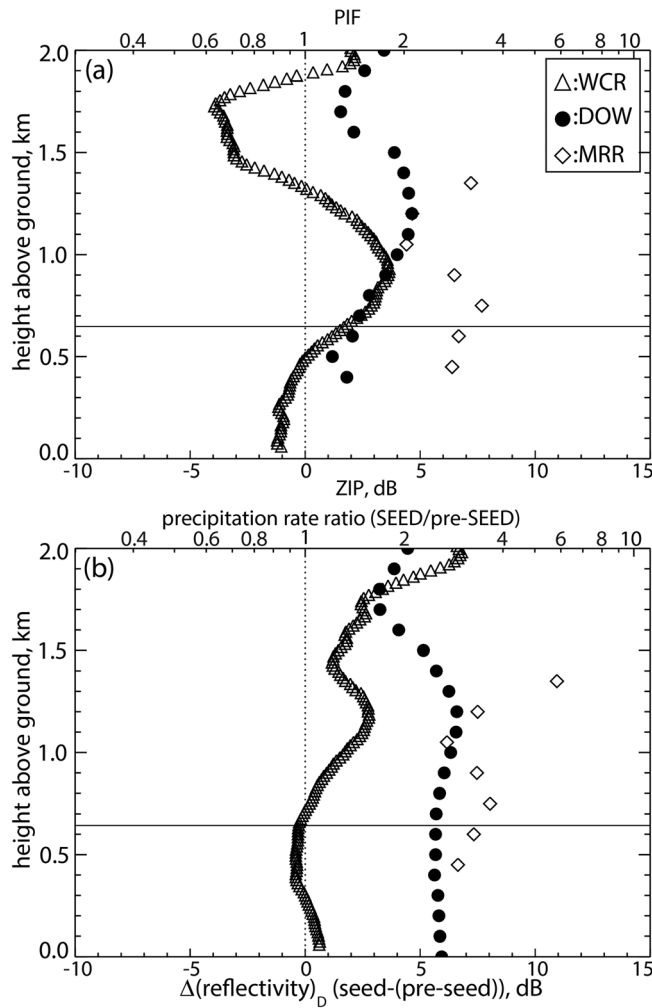


Figure 15. Vertical profiles of reflectivity difference parameters for three radar systems each with their own control and target regions. The upwind and lee target regions are combined for the DOW. (a) Double-difference parameters ZIP and PIF (defined in the text). (b) Single difference parameters in the target region. The vertical dotted line in both panels separates a positive effect to the right from a negative effect to the left. The horizontal solid line is the WCR-derived average PBL depth.

steadily during SEED (Figure 16a) and remains high in the post-SEED period, and only then decreases. Such persistence, after AgI seeding ceases, is consistent with MRR reflectivity time series (section 4.2) and has been observed in other ASCII case studies (PGJ14 and P14) and in at least one previous study, over the Sierra Nevada [Deshler and Reynolds, 1990]. Seeding plume analysis using both observations and modeling by Boe *et al.* [2014] and Xue *et al.* [2014], respectively, over a mountain in southeast Wyoming also shows that the seeding material may take up to 2 h to dissipate from the target region after ground-based seeding ceases. A delayed impact may be due to the slow mixing of the AgI nuclei into the cloud layer, a mean transport speed less than the mean wind (which we calculated from the sounding, between the surface and mountain top level), or a slow nucleation rate, as the AgI nuclei were released ~300 m below cloud base. The mean particle diameter shows a slight negative trend during SEED (Figure 16b).

The Parsivel particle size distribution data are grouped into three parts corresponding with the pre-SEED, SEED, and post-SEED periods and then composited as frequency by diameter displays (FDDs) (Figure 17). Particle concentration tends to drop off exponentially with size, as expected. The frequency of especially smaller particles was more diverse during pre-SEED, consistent with Figure 16a. Particle concentrations, mainly in the smaller size bins, generally are higher during SEED (Figure 17d) and into the post-SEED period (Figure 17e). Particles <1 mm in diameter are about twice as common during SEED and post-SEED,

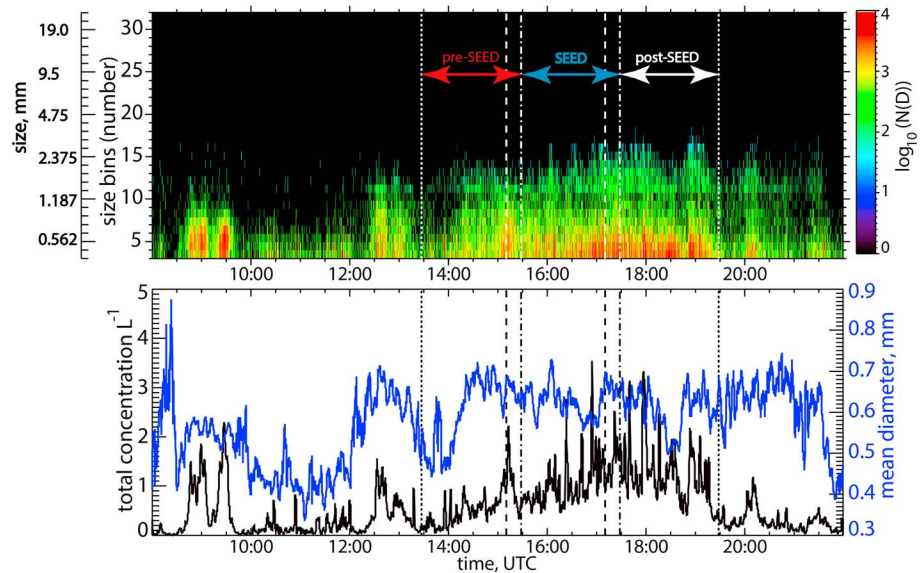


Figure 16. Time series of Parsivel disdrometer measurements at Battle Town site: (a) snow size distribution; (b) total snow concentration (black line) and mean diameter (blue line). The vertical dashed and dashed-dotted lines in both panels are as in Figure 9. The vertical dotted lines show the start/end time of the IOP.

compared to pre-SEED. Particles larger than 1.5 mm are more common as well in these periods. Particle concentrations declined again starting near the end of the post-SEED period (Figure 16a). This is consistent with the MRR reflectivity (not shown), which is the only other measurement available post-IOP. Particles have high fallspeeds, $\sim 2.5 \text{ m s}^{-1}$, in all periods (Figure 17f), and even higher for larger particles, confirming heavy riming. The fallspeed is slightly larger during SEED (continuing into post-SEED). This is consistent with the WCR hydrometeor vertical velocity (Figure 8e), which also shows slightly stronger particle subsidence during SEED. And, both observations are consistent with an increase in riming suggested by the decrease in DOW ZDR for most Z values during SEED (Figure 14).

6. Discussion

The orographic cloud sampled on 22 February 2012 was unusual in its abundance of large ($\sim 35 \mu\text{m}$) droplets, apparently the result of a warm cloud top ($\sim -12^\circ\text{C}$), strong wind shear, low droplet concentration ($\sim 40 \text{ cm}^{-3}$), and low ice concentration ($\sim 20 \text{ L}^{-1}$), notwithstanding conditions generally suitable for ice splintering (Hallett and Mossop, 1974). The cloud base was rather warm ($\sim -5^\circ\text{C}$) for AgI-mediated ice nucleation, but natural ice nuclei and thus ice crystals are rare at temperatures above -12°C [e.g., DeMott et al., 2010; Grant and Elliott, 1974], and there was no natural seeding from aloft. The orographic cloud also appeared to be well mixed by turbulence under strong wind. Thus, even though natural ice crystals and snowfall were present in the cloud before seeding commenced, this cloud was a suitable target for ground-based AgI seeding, and indeed, MRR and mainly DOW data show increased radar reflectivity during SEED.

This case is complicated because the storm naturally produced more LW (Figure 3e) and precipitation (Figures 12a and 9a) in the second half of the IOP during SEED. It is possible that the enhanced reflectivity increases in the DOW target region (Figures 12b and 13c) and over Battle Pass according to the MRR (Figure 10) (“enhanced” compared to the trend in the respective control regions) are natural: when a storm intensifies in the foothills region (i.e., the control region), then one can expect a larger increment over the mountain. This argument cannot be dismissed with the available data. Another argument against AgI-seeding impact may be that the positive ZIP values for the DOW and MRR (Figure 15a) are not confined below the top of the well-mixed PBL (as one would expect from ground-based seeding), but extend up toward echo top. This argument can be dismissed as follows: in this case convective-strength vertical motions were present over the depth of the cloud (Figure 8e). They may have carried AgI nuclei and even lightly rimed hydrometeors to cloud. A third argument against AgI-seeding impact may be that

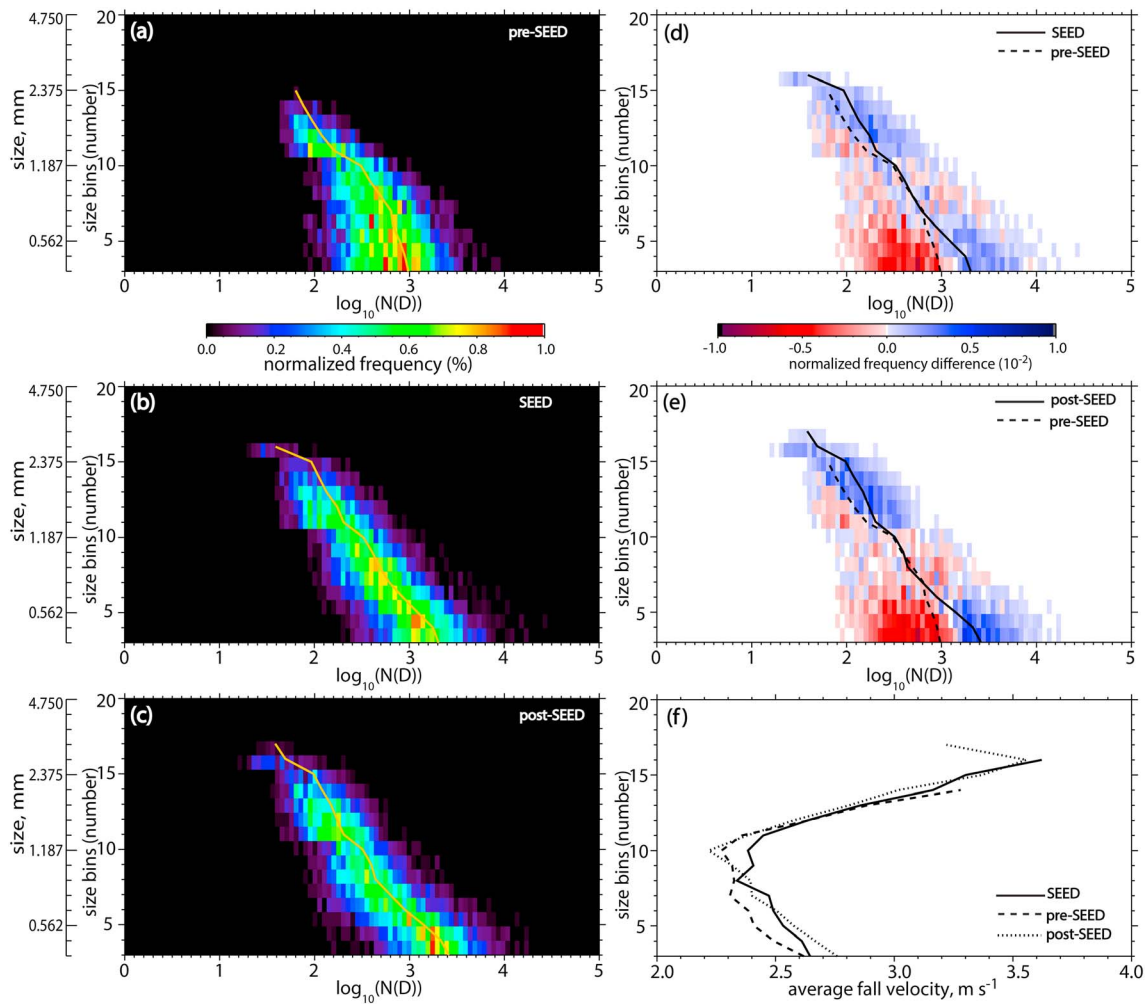


Figure 17. The left column shows the normalized frequency by diameter display (FDD) of snow particle concentration measured by the Parsivel at Battle Town site during (a) pre-SEED, (b) SEED, and (c) post-SEED. (d and e) The difference FDD (SEED – pre-SEED and post-SEED – pre-SEED, respectively) is also shown. The solid yellow lines in Figures 17a–17c show the average values; these lines are repeated as black lines in Figures 17d and 17e. (f) Average particle fall velocity measured by the Parsivel for the same three periods.

the surface wind at Battle Pass was quite strong, exceeding 10 m s^{-1} (Figure 3). This may have allowed near-surface blowing snow to mix into the cloud within the turbulent boundary layer, a natural source of ice crystals from the ground up [Rogers and Vali, 1987; Geerts et al., 2011; Vali et al., 2012], thereby reducing the impact of artificial seeding. This argument is possible, but unlikely since the denser rimed snow particles falling during this IOP are less likely to become airborne again after reaching the ground.

In general, it is almost impossible to unambiguously separate natural from seeding-induced changes based on observations alone. But in this case the evidence (mainly from the DOW, the MRR, and the Parsivel) suggests that AgI seeding increased the concentration of both small and large hydrometeors and thus the precipitation rate in the target region. In all likelihood AgI seeding increased the number of ice crystals, especially small crystals (Figure 17d). The snow growth enhancement may have been a combination of diffusional and accretional growth (“static seeding” [Bruitjes, 1999]). Any dynamic response (due to extra latent heat release) is not apparent as echo tops did not increase (Figure 12b) and the cloud layer was rather well capped (Figure 3).

With all data at hand at this stage in the paper, we revisit the question why the WCR does not show a positive seeding impact (Figure 8f and section 4.1), while the centimeter-wave radars (MRR and DOW) do (Figure 15b). There are three factors. First, this is due to the mismatch in SEED/pre-SEED periods (Table 1). The WCR SEED period ended prematurely at 16:37 UTC, just at the time when the radiometer LWP starts to double

(Figure 3e). The MRR (DOW) SEED period does not end until 51 min (76 min) later. If the SEED periods for the MRR (and DOW) are reduced to match that of the WCR, then the low-level ZIP values are halved, from 7 dB (3 dB) to 4 dB (1.5 dB). A secondary reason is a slight increase in LWP between the UWKA's pre-SEED and SEED periods (Figure 3e). As mentioned in section 3.5, Z_{WCR} needs to be corrected first for attenuation by liquid water, increasing it by ~ 2 dBZ during pre-SEED. The higher LWP during SEED implies that the mean Z_{WCR} near the ground should be another 0.5–1.0 dBZ higher.

The third and most important reason is that the concentration of large hydrometeors increased significantly during SEED in the target region, as shown in section 5. This enhances Z more for centimeter-wave radars than for a millimeter-wave radar. The disdrometer recorded mean hydrometeor diameter (D) during pre-SEED near 0.6 mm (Figure 16). This gives approximate size parameters ($x = \pi D/\lambda$) of $x_{DOW} = 0.06$ and $x_{WCR} = 0.6$ for the DOW and WCR, respectively (λ is radar wavelength). The former value is within applicability of Rayleigh scattering theory, but the latter is in the transition from Rayleigh to Mie regimes. A large fraction of particles scatter W-band radiation in the Mie regime. Mie theory predicts smaller scattering efficiencies relative to Rayleigh theory, with a difference that increases with particle diameter. This is the basis for dual-frequency radar estimates of particle diameter and precipitation rate [e.g., *Le and Chandrasekar, 2012*]. This largely explains the difference between Z_{DOW} (Figure 12) and Z_{WCR} (Figure 8). The dual-frequency ratio (Z_{DOW}/Z_{WCR} , expressed in dB units) in the lowest 500 m is about 14 dB in the target region, on average, during pre-SEED, based on Figures 8f and 12b. (Here we assess the WCR target tracks and the DOW upwind target region and ignore W-band liquid water correction.) This ratio increases to ~ 20 dB during SEED. This suggests that the increase in DOW low-level reflectivity during SEED, and lack thereof in terms of WCR reflectivity (Figure 15b), is mostly explained by an increase in concentration of large particles, as observed indeed at Battle Pass (Figure 17d). In short, the ZIP values of the centimeter-wave radars, especially the DOW, may more accurately represent the seeding impact.

7. Conclusions

This paper presents a case study of the impact of glaciogenic seeding on a shallow, naturally precipitating, orographic cloud with large supercooled droplets, observed on 22 February 2012 during the ASCII field experiment over the Sierra Madre in southern Wyoming. The cloud, confined between -5 and -12°C , was marked by abundant large ($\sim 35 \mu\text{m}$) droplets, resulting in rimed snow particles and graupel. Echoes were widespread over the mountain and contained small cells with strong updrafts, on account of the strong wind ($\sim 20 \text{ m s}^{-1}$). This resulted in effective vertical mixing over the depth of the cloud.

Data used in this analysis come from three different radar systems and from several in situ particle sizing and imaging probes on the ground and in the air. The impact of AgI seeding is studied by contrasting the measurements collected before seeding commenced (pre-SEED) against those during seeding (SEED), both in a target region and in an upwind control region. A higher than expected silver concentration was found in a fresh snow sample collected at Battle Town site in the target region during SEED, indicating that at least one of the AgI nuclei plumes (or AgI-impacted snow) probably reached that site.

The key conclusions are as follows:

1. A large number of AgI nuclei, released near the ground below cloud base, likely reached cloud base and even the upper parts of the shallow cloud, where it was cold enough for AgI-mediated ice nucleation.
2. Evidence for a positive impact of AgI seeding on surface precipitation rate comes from the centimeter-wave radars, and the Parsivel at Battle Town site. The DOW and MRR pair point to an increase in low-level reflectivity in the target region, after accounting for the natural trend as observed in the control region. The Parsivel disdrometer shows an increase in concentration of mainly small ice crystals ($D < 1 \text{ mm}$), but also large particles ($D > 1.5 \text{ mm}$) during SEED. This increase, as well as the changes observed by the MRR, continued at least 1 h after seeding ended, which is consistent with several other case studies.
3. Reflectivity values from a third radar, the airborne millimeter-wave WCR, do not show such increase, but they were affected by an increase in liquid water and in concentration of large particles scattering in the Mie regime, both of which suppress millimeter-wave reflectivity relative to that from centimeter-wave radars.
4. This case is complicated by a natural increase in cloud liquid water and precipitation rate during the second half of the SEED period. This led to an increase in snow growth by riming in the target region, as evidenced

by particle imaging data on the ground and by a decrease in DOW differential reflectivity (ZDR) for most values of reflectivity.

Follow-up work will examine a cloud-resolving numerical simulation of this case, i.e., a large eddy simulation with an inner-domain resolution of 100 m and an AgI cloud seeding parameterization [Xue *et al.*, 2013a, 2013b].

Acknowledgments

The data for this paper are available at the University of Wyoming King Air project site under <http://flights.uwyo.edu/projects/ascii12/>. The ASCII campaign is funded by the National Science Foundation grant AGS-1058426. This work also received funding from the Wyoming Water Development Commission grant 1001552C and the United States Geological Survey grant 10000628S, under the auspices of the University of Wyoming Water Research Program. The operation of the AgI generators, the upstream MRR, and the microwave radiometer was supported by the WWMPP, which is funded by the State of Wyoming and managed by Barry Lawrence. We thank Katja Friedrich for collecting and sharing MRR and Parsivel data from Battle Pass, Dan Breed for the MRR data collected at Ladder Livestock ranch, and Arlen Huggins for the trace analysis of snow samples collected at Battle Pass. The paper was much improved with the input of three anonymous reviewers.

References

- Austin, P. M. (1987), Relation between measured radar reflectivity and surface rainfall, *Mon. Weather Rev.*, *115*, 1053–1070.
- Boe, B. A., J. A. Heimbach, T. W. Krauss, L. Xue, X. Chu, and J. T. McPartland (2014), The dissipation of silver iodide particles from ground-based generators over complex terrain: Part I: Observations with acoustic ice nucleus counters, *J. Appl. Meteorol. Climatol.*, *53*, 1325–1341.
- Breed, D., R. Rasmussen, C. Weeks, B. Boe, and T. Deshler (2014), Evaluating winter orographic cloud seeding: Design of the Wyoming Weather Modification Pilot Project (WWMPP), *J. Appl. Meteorol. Climatol.*, *53*, 282–299, doi:10.1175/JAMC-D-13-0128.1.
- Bruinjtes, R. T. (1999), A review of cloud seeding experiments to enhance precipitation and some new prospects Bull, *Am. Meteorol. Soc.*, *80*, 805–820.
- Cooper, W. A., and G. Vali (1981), The origin of ice in mountain cap clouds, *J. Atmos. Sci.*, *38*, 1244–1259, doi:10.1175/1520-0469(1981)038.
- DeMott, P. J. (1997), Report to North Dakota Atmospheric Resource Board and Weather Modification Incorporated on tests of the ice nucleating ability of aerosols produced by the Lohse Airborne Generator, *Rep.*, 15 pp., Dep. Atmos. Sci., Colo. State Univ., Fort Collins.
- DeMott, P. J., A. J. Prennia, X. Liu, S. M. Kreidenweis, M. D. Petters, C. H. Twohy, M. S. Richardson, T. Eidhammer, and D. C. Rogers (2010), Predicting global atmospheric ice nuclei distributions and their impacts on climate, *Proc. Natl. Acad. Sci. U.S.A.*, doi:10.1073/pnas.0910818107.
- Deshler, T., and D. W. Reynolds (1990), The persistence of seeding effects in a winter orographic cloud seeded with silver iodide burned in acetone, *J. Appl. Meteorol.*, *29*, 477–488.
- Garstang, M., R. Bruinjtes, R. Serafin, H. Orville, B. Boe, W. Cotton, and J. Warburton (2005), Weather modification: Finding common ground, *Bull. Am. Meteorol. Soc.*, *86*, 647–655.
- Geerts, B., Q. Miao, and Y. Yang (2011), Boundary-layer turbulence and orographic precipitation growth in cold clouds: Evidence from profiling airborne radar data, *J. Atmos. Sci.*, *68*, 2344–2365.
- Geerts, B., B. Pokharel, K. Friedrich, D. Breed, R. Rasmussen, Y. Yang, Q. Miao, S. Haimov, B. Boe, and E. Kalina (2013), The AgI seeding cloud impact investigation (ASCI) campaign 2012: Overview and preliminary results, *J. Weather Modif.*, *45*, 24–43.
- Givati, A., and D. Rosenfeld (2005), Separation between cloud-seeding and air-pollution effects, *J. Appl. Meteorol.*, *44*, 1298–1314.
- Grant, L. O., and R. E. Elliott (1974), The cloud seeding temperature window, *J. Appl. Meteorol.*, *13*, 355–363.
- Griggs, D. J., and T. W. Chouarton (1986), A laboratory study of secondary ice particle production by the fragmentation of rime and vapour-grown ice crystals, *Q. J. R. Meteorol. Soc.*, *112*, 149–163.
- Hallett, J., and S. C. Mossop (1974), Production of secondary ice particles during the riming process, *Nature*, *249*, 26–28.
- Hobbs, P. V. (1975), The nature of winter clouds and precipitation in the Cascade Mountains and their modification by artificial seeding. Part I: Natural conditions, *J. Appl. Meteorol.*, *14*, 783–804.
- Houze, R. A. (1993), *Cloud Dynamics*, Academic, San Diego, Calif.
- Jing, X., B. Geerts, K. Friedrich, and B. Pokharel (2015), Dual-Polarization radar data analysis of the impact of ground-based glaciogenic seeding on winter orographic clouds, Part I: Mostly stratiform clouds, *J. Appl. Meteorol. Climatol.*, doi:10.1175/JAMC-D-14-0257.1, in press.
- Kirschbaum, D. J., and D. R. Durran (2004), Factors governing cellular convection in orographic precipitation, *J. Atmos. Sci.*, *61*, 682–698.
- Korolev, A. V., and G. A. Isaac (1999), Ice particle habits in Arctic clouds, *Geophys. Res. Lett.*, *26*(9), 1299–1302, doi:10.1029/1999GL000232.
- Lance, S., C. A. Brock, D. Rogers, and J. A. Gordon (2010), Water droplet calibration of the Cloud Droplet Probe (CDP) and in-flight performance in liquid, ice and mixed-phase clouds during ARCPAC, *Atmos. Meas. Tech.*, *3*, 1683–1706, doi:10.5194/amt-3-1683-2010.
- Lawson, R. P., B. A. Baker, P. Zmarzly, D. O'Connor, Q. Mo, J. F. Gayet, and V. Shcherbakov (2006), Microphysical and optical properties of atmospheric ice crystals at South Pole Station, *J. Appl. Meteorol. Climatol.*, *45*, 1505–1524.
- Le, M., and V. Chandrasekar (2012), Raindrop size distribution retrieval from dual-frequency and dual-polarization radar, *Geosci. Remote Sens., IEEE Trans.*, *50*, 1748–1758, doi:10.1109/TGRS.2011.2167683.
- Li, Z., and R. L. Pitter (1997), Numerical comparison of two ice crystal formation mechanisms on snowfall enhancement from ground-based aerosol generators, *J. Appl. Meteorol.*, *36*, 70–85.
- Locatelli, J. D., and P. V. Hobbs (1974), Fall speeds and masses of solid precipitation particles, *J. Geophys. Res.*, *79*, 2185–2197, doi:10.1029/JC079i015p02185.
- Löffler-Mang, M., and J. Joss (2000), An optical disdrometer for measuring size and velocity of hydrometeors, *J. Atmos. Oceanic Technol.*, *17*, 130–139.
- Long, A. B., and A. W. Huggins (1992), Australian Winter Storms Experiment (AWSE) I: Supercooled liquid water and precipitation-enhancement opportunities, *J. Appl. Meteorol.*, *31*, 1041–1055, doi:10.1175/1520-0450(1992)031.
- Lundqvist, H., K. Muinonen, T. Nousiainen, J. Um, G. M. McFarquhar, P. Haapanala, R. Makkonen, and H. Hakkarainen (2012), Ice-cloud particle habit classification using principal components, *J. Geophys. Res.*, *117*, D16206, doi:10.1029/2012JD017573.
- Maahn, M., and P. Kollias (2012), Improved Micro Rain Radar snow measurements using Doppler spectra post-processing, *Atmos. Meas. Tech.*, *5*, 2661–2673.
- Matrosov, S. Y. (2007), Modeling backscatter properties of snowfall at millimeter wavelengths, *J. Atmos. Sci.*, *64*, 1727–1736.
- National Research Council (2003), *Critical Issues in Weather Modification Research*, 123 pp., Natl. Academy Press, Washington, D. C.
- Pobanz, B. M., J. D. Marwitz, and M. K. Politovich (1994), Conditions associated with large-drop regions, *J. Appl. Meteorol.*, *33*, 1366–1372.
- Pokharel, B., B. Geerts, and X. Jing (2014a), The impact of ground-based glaciogenic seeding on orographic clouds and precipitation: A multi-sensor case study, *J. Appl. Meteorol. Climatol.*, *53*, 890–909, doi:10.1175/JAMC-D-13-0290.1.
- Pokharel, B., B. Geerts, X. Jing, K. Friedrich, J. Aikins, D. Breed, R. Rasmussen, and A. Huggins (2014b), The impact of ground-based glaciogenic seeding on clouds and precipitation over mountains: A multi-sensor case study of shallow precipitating orographic cumuli, *Atmos. Res.*, *147–148*, 162–182, doi:10.1016/j.atmosres.2014.05.014.
- Politovich, M. K. (1989), Aircraft icing caused by large supercooled droplets, *J. Appl. Meteorol.*, *28*, 856–868.
- Politovich, M. K., and G. Vali (1983), Observations of liquid water in orographic clouds over Elk Mountain, *J. Atmos. Sci.*, *40*, 1300–1312, doi:10.1175/1520-0469(1983)040.
- Pruppacher, H. R., and J. D. Klett (1997), *Microphysics of Clouds and Precipitation*, 954 pp., Kluwer, Dordrecht, Netherlands.

- Rangno, A. L., and P. V. Hobbs (1983), Production of ice particles in clouds due to aircraft penetrations, *J. Climate Appl. Meteorol.*, *22*, 214–232.
- Rasmussen, R., M. Dixon, S. Vasiloff, F. Hage, S. Knight, J. Vivekanandan, and M. Xu (2003), Snow nowcasting using a real-time correlation of radar reflectivity with snow gauge accumulation, *J. Appl. Meteorol.*, *42*, 20–36.
- Rauber, R. M., and L. O. Grant (1987), Supercooled liquid water structure of a shallow orographic cloud system in southern Utah, *J. Climate Appl. Meteorol.*, *26*, 208–215, doi:10.1175/1520-0450(1987)026.
- Rauber, R. M., and A. Tokay (1991), An explanation for the existence of supercooled water at the top of cold clouds, *J. Atmos. Sci.*, *48*, 1005–1023, doi:10.1175/1520-0469(1991)048.
- Rogers, D. C., and G. Vali (1987), Ice crystal production by mountain surfaces, *J. Climate Appl. Meteorol.*, *26*, 1152–1168.
- Sand, W. R., W. A. Cooper, M. K. Politovich, and D. L. Veal (1984), Icing conditions encountered by a research aircraft, *J. Climate Appl. Meteorol.*, *23*, 1427–1440.
- Sassen, K., R. M. Rauber, and J. B. Snider (1986), Multiple remote sensor observations of supercooled liquid water in a winter storm at Beaver, Utah, *J. Clim. Appl. Meteorol.*, *25*, 825–834, doi:10.1175/1520-0450(1986)025.
- Steenburgh, J. (2014), *Secrets of the Greatest Snow on Earth: Weather, Climate Change, and Finding Deep Powder in Utah's Wasatch Mountains and Around the World*, Utah State Univ. Press, Logan, Utah.
- Vali, G., and S. Haimov (1999), Observed extinction by clouds at 95 GHz, *IEEE Trans. Geosci. Remote Sens.*, *39*, 190–193.
- Vali, G., D. Leon, and J. R. Snider (2012), Ground-layer snow clouds, *Q. J. R. Meteorol. Soc.*, *138*, 1507–1525.
- Wang, J. Y., and B. Geerts (2003), Identifying drizzle within marine stratus with W-band radar reflectivity profiles, *Atmos. Res.*, *69*, 1–27.
- Wang, P. K., and W. Ji (2000), Collision efficiencies of ice crystals at low-intermediate Reynolds numbers colliding with supercooled cloud droplets: A numerical study, *J. Atmos. Sci.*, *57*, 1001–1009.
- Wang, Z., et al. (2012), Single aircraft integration of remote sensing and in situ sampling for the study of cloud microphysics and dynamics, *Bull. Am. Meteorol. Soc.*, *93*, 653–668.
- Xue, L., A. Hashimoto, M. Murakami, R. Rasmussen, S. Tessendorf, D. Breed, S. Parkinson, P. Holbrook, and D. Blestrud (2013a), AgI cloud seeding effects as seen in WRF simulations. Part I: Model description and idealized 2D sensitivity tests, *J. Appl. Meteorol. Climatol.*, *52*, 1433–1457.
- Xue, L., S. Tessendorf, E. Nelson, R. Rasmussen, D. Breed, S. Parkinson, P. Holbrook, and D. Blestrud (2013b), AgI cloud seeding effects as seen in WRF simulations. Part II: 3D real case simulations and sensitivity tests, *J. Appl. Meteorol. Climatol.*, *52*, 1458–1476.
- Xue, L., X. Chu, R. Rasmussen, D. Breed, B. Boe, and B. Geerts (2014), The dissipation of silver iodide particles from ground-based generators over complex terrain: Part II: WRF Large-Eddy simulations versus observations, *J. Appl. Meteorol. Climatol.*, *53*, 1342–1361.
- Yuter, S., and R. A. Houze (1995), Three-dimensional kinematic and microphysical evolution of Florida cumulonimbus. Part II: Frequency distributions of vertical velocity, reflectivity, and differential reflectivity, *Mon. Weather Rev.*, *123*, 1941–1963.
- Yuter, S. E., D. E. Kingsmill, L. B. Nance, and M. Löffler-Mang (2006), Observations of precipitation size and fall speed characteristics within coexisting rain and wet snow, *J. Appl. Meteorol. Climatol.*, *45*, 1450–1464.
- Zipori, A., D. Rosenfeld, J. Shpund, D. M. Steinberg, and Y. Erel (2012), Targeting and impacts of AgI cloud seeding based on rain chemical composition and cloud top phase characterization, *Atmos. Res.*, *114–115*, 119–130.